KTH Land and Water Resources Engineering

REACTIVE TRANSPORT MODELLING OF DISSOLVED CO_2 IN POROUS MEDIA

Injection into and leakage from geological reservoirs

Nawaz Ahmad

April 2016

TRITA-LWR PhD-2016:04
ISSN 1650-8602
ISBN 978-91-7595-911-5

PhD Thesis
Doctoral program in Land and Water Resources Engineering
School of Architecture and the Built Environment
KTH Royal Institute of Technology
SE-100 44 STOCKHOLM, Sweden
Reference to this publication should be written as: Ahmad, N. 2016. Reactive transport modelling of dissolved CO_2 in porous media: Injection into and leakage from geological reservoirs. PhD Thesis, TRITA-LWR PhD-2016:04, 59 p.

Dedicated to my parents (late) and eldest sister.

ABSTRACT

The geological sequestration of carbon dioxide (CO_2) is seen as one of the options of mitigating the imbalance of greenhouse gas emissions and to avoid global warming. However, leakage of CO_2 from the subsurface storage reservoir is a potential long-term process with consequences for the bio- and hydrosphere. Over longer times, large-scale groundwater motion may displace the brine out of the storage reservoir with associated leakage risk of dissolved CO_2 (CO_{2aq}) along the conducting pathways.

The objectives of this thesis are twofold. First, the modelling study analyzes the leakage of CO_{2aq} along the conducting pathways in caprock. Second, a relatively safer mode of geological storage is investigated wherein CO_2 dissolved in brine is injected in a carbonate reservoir. A reactive transport model and computer code is developed that accounts for the coupled hydrological transport and the geochemical reactions of CO_{2aq} in the subsurface porous media. Advection, dispersion, diffusion into the rock matrix, sorption and geochemical reactions are considered along the leakage pathway. The study provides a quantitative assessment of the impact of advection, dispersion, diffusion, sorption, geochemical reactions, temperature, and heat transport on the fate of CO_{2aq} leaking from the reservoir.

The mass exchange between the principal conducting pathway and the rock matrix through matrix diffusion plays an important role in providing extra space for retention and reactions of leaking CO_{2aq} along the travel pathway. A significant retention of leaking CO_{2aq} is caused by its mass stored in aqueous and adsorbed states and its consumption in reactions in the rock matrix along the leakage pathway. Under some plausible conditions for clay-rich caprock, the results demonstrate that advection can cause a significant leakage of CO_{2aq} directly from the reservoir through the matrix in comparison to the diffusion alone in the rock matrix and advection along a highly conducting, but thin fracture. The analysis also demonstrated how geochemical reactions successively changed the porosity and permeability of the medium along the leakage pathway. Hence, the combination of advection, dispersion, diffusion, sorption, geochemical reactions, temperature and heat transported by leaking brine along the transport pathway are found key for understanding the fate of leaking CO_{2aq} from the reservoir.

Injection of CO_2 dissolved in brine was simulated for a carbonate reservoir. Injected CO_2-saturated brine being reactive causes fast dissolution of carbonate minerals in the reservoir and fast conversion of CO_{2aq} into other ions (ionic trapping) through considered geochemical reactions. Various parameters like dispersion, sorption, temperature, and minerals reaction kinetics are found to play important role in the consumption of CO_{2aq} in reactions.

Key words: CO_2 geological storage and safety; leakage of brine saturated with dissolved CO_2; reactive transport; fracture; advection, dispersion and diffusion; sorption; carbonate minerals kinetic reactions; calcite; dolomite; siderite; porosity; permeability; heat transport

ACKNOWLEDGMENTS

Foremost, I am thankful to the Higher Education Commission (HEC) of Pakistan, KTH Royal Institute of Technology, Lars Erik Lundberg Scholarship Foundation, Sweden and STandUp for Energy, the national strategic research project for funding this research work. Special thanks go to my employer Ministry of Petroleum & Natural Resources, government of Pakistan for granting me the study leave for higher education.

I would like to express my sincere gratitude to my Principal Advisor Professor Anders Wörman, for his great contribution in completion of my PhD. I found him always very welcoming, encouraging and supportive in personal and administrave matters. I am also thankful to my co-advisor Professor Vladimir Cvetkovic for his motivation and encouragement.

Many thanks go to Associate Professor Xavier Sanchez-Vila, UPC Spain for his co-authoring of the Papers. Without his scientific contribution completion of my PhD would have been more challenging. I am greatful to Dr. Andrea Bottacin-Busolin, University of Manchester, UK for his dedicated support, co-authoring all the Papers and contributing in writing PhD thesis. He was always available to help whenever it was needed. I am also thankful to my other co-authors Associate Professor Jerker Jarsjö, Stockholm University, Sweden and Dr. Helge Hellevang, University of Oslo, Norway for their scientific contributions in two of the Papers.

I am greatful to Prof. Jon-Petter Gustafsson for his Quality Review of the thesis and recommending valuable modifications. Many thanks go to Aira Saarelainen, Britt Chow, Merja Carlqvist, Sofia Jonsson and Sari Nieminen for their active support in solving the PhD administrative matters. I cannot go without acknowledging Jerzy Buczak for his timely IT related support. All my Pakistani friends in Sweden particularly Muhammad Shaban, Zahid Anwar and Muhammad Afzal made my times very happy and memorable.

I am thankful to the colleagues here at KTH for their help and nice company. Special mention goes to Bijan Dargahi, Hans Bergh, Proson Bhattacharya, Gunnar Jacks, Roger Thunvik, Anna Åkesson, Joakim Riml, Ting Liu, Farzad Ferdos, Nicholas Zmijewski, Ida Morén and Fredrik Illerstam.

I would like to dedicate my PhD to my Parents (late) for sacrificing their lives in educating us all brothers and sisters despite hard economic conditions. Deepest gratitudes go to my Mother Zubaida Begum who fought the illness for long and passed away in 2015. Heartfelt thanks go to my brothers, sisters and wife for their love, support and encouragement. Special thanks and deepest love go to my loving kids Imaan Fatima and Hasssaan Ahmad Virk for their long wait and allow me complete my PhD.

Nawaz Ahmad
March, 2016, Stockholm Sweden

LIST OF APPENDED PAPERS

This thesis comprises following four papers:

I. **Ahmad N**., Wörman A., Bottacin-Busolin A., Sanchez-Vila X., 2015. Reactive transport modeling of leaking CO_2-saturated brine along a fractured pathway. *Int. J. Greenhouse Gas Cont.* **(42),** 672-689.

II. **Ahmad N**., Wörman A., Sanchez-Vila X., Bottacin-Busolin A. The role of advection and dispersion in the rock matrix on the transport of leaking CO_2-saturated brine along a fractured zone. Submitted to *Advances in Water Resources*.

III. **Ahmad N**., Wörman A., Jarsjö J., Sanchez-Vila X., Bottacin-Busolin A., Hellevang H. Non-isothermal reactive transport modelling of dissolved CO_2 leaking through a fractured caprock. Submitted to *Water Resources Research*.

IV. **Ahmad N**., Wörman A., Sanchez-Vila X., Jarsjö J., Bottacin-Busolin A., Hellevang H. Injection of CO_2-saturated brine in geological reservoir: A way to enhanced storage safety. Submitted to *International Journal of Greehouse Gas Control*.

Contribution of the author in the papers:

(i) Development of geochemical code and its implementation in COMSOL Multiphysics® simulator.
(ii) Scientific planning, theoretical development, modelling, evaluation and most of the writing.

Related work not included in the thesis:

Ahmad N., Wörman A., Bottacin-Busolin A., 2013. Numerical modeling of CO_2 brine leakage and evolution of two-phase flow. American Geophysical Union (AGU), Fall Meeting 9-13 December, 2013, San Francisco, CA, USA.

Table of contents

1. INTRODUCTION

Continued human activities, such as the burning of fossil fuels and unsustainable land uses, have resulted in significant emissions of carbon dioxide (CO_2) and other greenhouse gases (GHG) into the atmosphere. Despite remarkable growth in renewable energies, concentrations of CO_2 in the atmosphere will likely continue to increase because of the continued use of fossil fuels (Bachu and Adam, 2003; Orr, 2009a). The global warming linked to the emissions of greenhouse gases into the atmosphere has caused severe global impacts on the environment and biota (Fields et al., 1993; Orr, 2009a; Wolf-Gladrow et al., 1999). The global emissions can be significantly reduced by storing CO_2 in subsurface geological reservoirs instead of releasing it into the atmosphere (Orr, 2009b).

1.1. CO_2 geological storage

Geological sequestration of CO_2 has been seen as a promising way to mitigate the potential future global warming (Holloway, (1997, 2005); IPCC, 2002; Middleton et al., 2012). CO_2 is captured from major emission sources, such as fossil fuel-fired power plants, and transported via a pipeline for its injection as a supercritical free-phase in a subsurface reservoir. CO_2 can be stored in three main types of geological structures (Holloway, 1997; Orr, 2009b): (i) saline aquifers, (ii) depleted oil or gas fields, and (iii) un-mineable coal seams. Deep aquifers containing highly saline brine are thought to be the best candidate for CO_2 geological sequestration due to their high volumetric capacity and worldwide abundance. CO_2 is injected as a supercritical free-phase to sequester its bulk quantities, but this option is associated with potential leakage risks over the geological time scale (Haugan and Joos, 2004; Stone et al., 2009). Fig. 1 shows the schematic of processes involved in CO_2 injection in subsurface geological storage reservoirs.

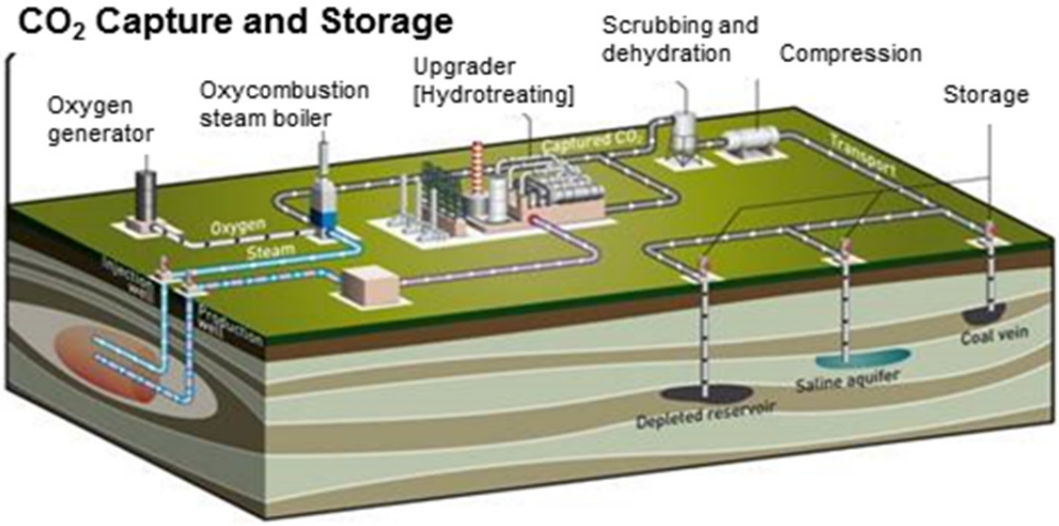

Fig. 1. Schematic of the processes involved in CO_2 geological disposal (Courtesy of TOTAL).

1.2. The ways CO_2 is stored in a geological reservoir

Injected supercritical free-phase CO_2 moves upward and accumulates beneath the overlying less-permeable caprock due to its lower density compared to that of the resident brine (Orr, (2009a, 2009b); Pool et al., 2013). Thus, the injection of free-phase CO_2 is performed in subsurface reservoirs covered with overlying less permeable caprock to stop its vertical movement and trap it in the reservoir below the caprock (García, 2003). The storage of injected CO_2 in the reservoir can be classified into two main categories; physical and chemical (IPCC, 2005). Structural trapping is a form of physical trapping where the free-phase CO_2 is trapped under very-low-permeable caprock (IPCC, 2005). Hydrodynamic trapping is another form of physical trapping where injected CO_2 stays as a free-phase in the pore spaces of deep aquifers (IPCC, 2005). Solubility, ionic and mineral trapping are considered forms of chemical trapping. Injected free-phase CO_2 dissolves in the reservoir fluid (solubility trapping), is converted into other carbon-bearing ionic species (ionic trapping) and is finally permanently consumed through mineral reactions (mineral trapping) (Zhang and Song, 2014; IPCC, 2005). Hydrodynamic trapping is the major form of CO_2 storage over short periods of time, followed by solubility trapping (tens to hundreds of years) and ionic trapping (hundreds to thousands of years), whereas mineral trapping spans over thousands to millions of years (Audigane et al., 2007; IPCC, 2005).

Dissolution between injected free-phase CO_2 and the resident formation fluid occur only at the CO_2-brine interface (Orr, (2009a, 2009b)). The resulting brine, containing dissolved CO_2, becomes slightly denser than the original brine and starts moving downwards in the reservoir, resulting in enhanced dissolution and reduced leakage risk over the period of time (Weir et al., 1996; IPCC, 2005; Audigane et al., 2007). Dissolved CO_2 decreases the pH of the resident fluid, making it more reactive with the minerals in the subsurface reservoir (Xu et al., (2003, 2004); Audigane et al., 2007). Various aqueous-mineral geochemical reactions driven by dissolved CO_2 cause minerals to either dissolve or precipitate, causing variations in the porosity and permeability of the subsurface porous media (Xu et al., 2003). As a result of geochemical reactions, dissolved CO_2 is converted into other carbon-bearing ions (ionic trapping), followed by its permanent consumption in various mineral reactions (mineral trapping) (IPCC, 2005; Audigane et al., 2007). Audigane et al. (2007) have reported a conversion of only 30% of injected CO_2 in the dissolved phase after 1000 years, whereas it took 10,000 years for complete dissolution of injected CO_2 in the reservoir. These authors have also reported that only 5% of injected free-phase CO_2 is consumed in mineral reactions over a period of 10,000 years. Thus, over a period of time and as a result of various types of trapping processes, including solubility, ionic, and mineral trapping, the quantities of injected free-phase CO_2 continue to decrease in the reservoir.

1.3. Leakage risk of injected CO_2 from a geological reservoir

The greatest risk of leakage is associated with free-phase CO_2 being low in density and buoyant with respect to the resident fluids in the reservoir (Weir et al., 1996; Xu et al., 2003; IPCC, 2005; Xu et al., 2007; Audigane et al., 2007; Leonenko and Keith, 2008). Existing weaker zones, such as fractures or faults, that are not detected at the time of reservoir selection or new weaker zones developed by reservoir pressure increase as a result of the CO_2 injection process, and subsurface tectonic activity may provide pathways for the leakage of buoyant free-phase CO_2. Pressure variations due to subsurface large-scale groundwater motions can also cause the leakage of free-phase CO_2 from the storage reservoir over longer time-scales. Thus, leakage of CO_2 is one of the major concerns related to the geological storage of CO_2 (Haugan and Joos, 2004; Stone et al., 2009).

Although the dissolution of CO_2 in the resident brine makes it slightly denser than the original brine, with a resulting downward convection in the reservoir, the risk of denser brine that contains dissolved CO_2 also exists due to large-scale groundwater motion over longer periods of time. Large-scale groundwater motion may cause pressure variations in the reservoir, resulting in the leakage of CO_2-charged brine along existing or pressured-induced fractures and faults (IPCC, 2005). Leakage of dissolved CO_2 may also take place as a result of the bulk displacement of brine carrying dissolved CO_2 along the direction of movement of groundwater (Gaus, 2010).

1.4. Physical and geochemical interactions of CO_2 with porous media along the leakage pathway

Although the fluid flow takes place mainly in highly conducting zones, such as fractures and faults, the adjacent less-permeable rock matrix also plays an important role in the solute transport in the fractured porous media (Grisak and Pickens, 1980). Mass exchanges can take place between the principal transport pathway (fractures or conducting fault zones) and the relatively less permeable adjacent rock matrix. Various physical and geochemical processes between the solute mass species and the porous media can take place, thus inhibiting the transport of the solute mass species in the fractured rocks. Significant retardation in the species transport may result from various physical and geochemical interactions of transporting species with the porous media along the flow pathway (Neretnieks, 1980; Cvetkovic et al., 1999; Xu et al., 2001; Bodin et al., 2003).

In the event that leakage of CO_2 from the storage reservoir takes place, either as a free-phase or as a dissolved phase, the leaking CO_2 may undergo various physical and geochemical processes along the transport pathway. The leaking CO_2 may dissolve in the fluid and undergo various geochemical reactions along the leakage pathway (Gaus et al., 2005; Gherardi et al., 2007; Ellis et al., 2011a; Nogues et al., 2013). Pore spaces of porous media may store dissolved CO_2. Sorption processes may fix CO_2 in the sorbed phase on the mineral surfaces along the leakage pathways. Various

geochemical reactions driven by the concentration of dissolved CO_2 may also consume quantities of dissolved CO_2 through its conversion into ions, such as H_2CO_3, HCO_3^-, and CO_3^{2-} (Kaufmann and Dreybrodt, 2007), followed by subsequent permanent removal in the form of precipitated carbonate minerals along the leakage pathway (Gaus et al., 2005). Mineral dissolution driven by dissolved CO_2 may release ions such as Na^+, Ca^{2+}, Mg^{2+}, and Fe^{2+}. These ions can form aqueous complexes, such as $NaHCO_{3aq}$, $CaHCO_3^+$, $MgHCO_3^+$, and $FeHCO_3^+$, by utilizing the bicarbonate ions available in the solution through the conversion of dissolved CO_2. Kaufmann and Dreybrodt (2007), via diffusive-reactive transport modelling, have reported the conversion of dissolved CO_2 into H^+ and HCO_3^- species in a ternary CO_2-H_2O-$CaCO_3$ system. Gaus et al., 2005 have found consumption and related retardation in the transport of dissolved CO_2 in their diffusive-reactive transport modelling performed for the lower part of the caprock. Thus, the interplay between the leakage pathway and the rock matrix is important for understanding the transport and fate of CO_2 leaking from the reservoir.

Geochemical reactions between the leaking brine carrying dissolved CO_2 and the minerals may cause geochemical alterations along the leakage pathway (Nogues et al., 2013). The leakage of low-pH brine has the potential to react with the host rock minerals, and it may cause variations in porosity and permeability of the medium along the flow pathway and influence the flow velocities. The variations in porosity and permeability along the flow pathway may either enhance the transport of leaking CO_2 due to the increase in hydraulic conductivity resulting from mineral dissolution or slow the transport processes as a consequence of the decrease in medium permeability linked to the mineral precipitation (Gaus, 2010). For example, a carbonate rock-forming mineral may undergo fast dissolution and widen the existing flow path (Gaus, 2010).

1.5. Injection of dissolved CO_2 in the geological reservoir to reduce the leakage risk

Dissolution of CO_2 in the resident brine of the reservoir increases the density of the resulting brine by approximately 1% (Bachu and Adams, 2003; Song et al., 2005; Duan et al., 2008; Zhang et al., 2011; Li et al., 2011). However, this increase in density resulting from CO_2 dissolution depends on pressure, temperature and salinity conditions. The resulting denser brine tends to settle downwards in the storage reservoir. Thus, the risk of CO_2 leakage is generally reduced once it is dissolved in the resident brine. Migration and leakage of CO_2 in the dissolved phase can only take place due to regional groundwater movement (IPCC, 2005). Deep subsurface groundwater moves very slowly, with velocities on the order of millimetres to centimetres per year (Bachu et al., 1994).

Therefore, the leakage risk associated with injected supercritical free-phase CO_2 in the subsurface reservoir can be reduced to a greater extent by injecting CO_2 in the dissolved phase (CO_{2aq}) instead of its free-phase (Aradóttir et al., 2012; Pool et al., 2013;

Gislason and Oelkers, 2014). The increase in the density of brine containing CO_{2aq} also makes it possible to inject CO_2 in its dissolved phase in subsurface reservoirs without the presence of overlying caprock (Gislason and Oelkers, 2014). Relatively shallow subsurface reservoirs can also be selected for the injection of CO_{2aq} (Aradóttir et al., 2012). An immediate consumption of injected CO_{2aq} can take place through solubility and ionic trapping (Gislason and Oelkers, 2014). Additionally, relatively fast permanent removal of CO_2 through mineral trapping can be expected for CO_{2aq} injected in the reservoir (Aradóttir et al., 2012). In the event of leakage of CO_{2aq}, it is less likely to reach the land surface due to its very slow movement, its significant retention caused by its mass being stored in aqueous and adsorbed states, and its conversion/consumption in various geochemical reactions along the travel pathways.

1.6. Rationale of the thesis

1.6.1. Reactive transport of leaking dissolved CO_2 along the fractured pathway

To date, no specific studies reported in the literature have analysed the retention and consumption of leaking CO_{2aq} along a fractured pathway based on physio-geochemical processes coupling mass exchanges between the conducting pathway and the surrounding less-permeable rock matrix.

Gherardi et al. (2007) have performed reactive transport modelling in the reservoir caprock for leaking free-phase CO_2 and the associated dissolved CO_2 in the brine. These authors have found porosity variations near the reservoir-caprock interface mainly due to reactions of mineral calcite. The experimental studies of Andreani et al. (2008) show an approximately 50% increase in porosity in close proximity to the fracture, mainly due to calcite dissolution caused by cyclic flows of the free-phase CO_2 and CO_2-saturated brine. Gaus et al. (2005) have performed diffusive-reactive numerical modelling of dissolved CO_2 diffusing from the reservoir into the overlying caprock. These authors report a 2.8% decrease in porosity in the lower part of the caprock (within approximately 2 m of the reservoir-caprock interface) due to the precipitation of the minerals calcite and kaolinite associated with the dissolution of the mineral anorthite after a period of 3000 years. Nogues et al. (2013), in their reactive transport modelling, have analysed the evolution of porosity and permeability at the pore-scale level driven by inflowing CO_2-saturated water. These authors have suggested that the geochemical modelling can be simplified by not including minerals, such as kaolinite, anorthite, and albite, where the carbonate minerals are present in abundance. Ellis et al. (2011a), in their experimental study performed for a period of seven days, investigated the geochemical evolution of fracture in carbonate rock due to geochemical interactions with flowing CO_2-acidified brine. Ellis et al. (2011a, 2011b) have found an increase in fracture aperture mainly due to calcite dissolution. Only a few experimental and simplified numerical modelling studies have been published thus far focusing on the geochemical

interactions of CO_2–acidified brine (Gaus, 2010). Gaus (2010) has thus identified the need to perform numerical modelling for the leakage of brine carrying dissolved CO_2 from the storage reservoir towards shallow depths to understand the related environmental impacts. Thus, to bridge the existing knowledge gap and investigate the fate of leaking CO_{2aq}, this study focuses on the numerical simulation of the reactive transport of brine carrying CO_{2aq} along a fractured pathway.

1.6.2. Injection of dissolved CO_2 in a geological reservoir

The injection of CO_2 in its dissolved phase has been proposed to increase the security of its geological sequestration (Aradóttir et al., 2012; Pool et al., 2013; Gislason and Oelkers, 2014). However, thus far, few numerical studies related to reactive transport modelling of injected dissolved-phase CO_2 and quantification of its transformation through geochemical reactions have been published (e.g., Aradóttir et al., 2012). Pool et al. (2013), in their numerical modelling, injected CO_{2aq} in the aquifer without considering its geochemical interactions with minerals. Thus, to augment the understanding and complement the existing studies on the subject, this work also focuses on the injection of CO_{2aq} and quantifies its transformation through geochemical reactions in the carbonate reservoir.

2. RESEARCH OBJECTIVES

The aims of this PhD thesis are twofold. First, the study focuses on the reactive transport modelling of CO_{2aq} leaking from geological storage reservoirs. The overall aim is quantification of the mass stored in aqueous and adsorbed states and consumed in reactions of leaking CO_{2aq} along a fractured pathway (Papers I-III). The following are the specific objectives of the individual Papers I-III:

- Investigate the role of physical and geochemical transport processes on the transport of leaking CO_{2aq} along the fractured pathway using a simplified model that considers only diffusion in the rock matrix (Paper I).
- Investigate how advection in the rock matrix affects different physical and geochemical transport processes influencing the fate of leaking CO_{2aq} along the fractured pathway (Paper II).
- Investigate the role of additional geochemical reactions, temperature and heat transport on the leaking CO_{2aq} along the fractured pathway (Paper III).

The study also investigates a relatively safer approach of CO_2 geological disposal where it is injected in its dissolved phase in shallow carbonate reservoir. Reactive transport modelling is performed considering physical and geochemical interactions of the injected CO_{2aq} in the carbonate reservoir. The objectives of Paper IV are:

- To quantify the mass stored in aqueous and adsorbed states and consumed in reactions of CO_{2aq} injected in the

carbonate reservoir. The roles of dispersion, temperature and pH-dependent mineral reaction kinetics are also investigated.

3. METHODOLOGY

3.1. Model approach and numerical solution

In this study, geochemical code was developed and implemented in COMSOL, which is a finite element-based multiphysics simulator, to perform the batch and reactive transport modelling. Flow and transport were coupled with geochemistry while taking into account the spatial and temporal variations in medium porosity and permeability resulting from mineral dissolution and precipitation. The developed geochemical code is capable of solving the geochemical reactions system (equilibrium plus mineral kinetics), updating the minerals' reactive surface area and tracking the variations in porosity and permeability. MATLAB was externally coupled with COMSOL to compute the density and viscosity of the brine fluid as well as fugacity and the activity coefficients of dissolved CO_2. MATLAB is a language and interactive environment used for technical computing. These variables were solved as a function of pressure, temperature and the concentration of aqueous species. The variables shared between COMSOL and MATLAB are updated every iteration. Fig. 2 presents a schematic of the coupling between COMSOL with MATLAB.

The reactive transport problem of mobile species was formulated in terms of chemical component species (u) that are the linear combination of aqueous species concentrations involved in geochemical reactions. The mass of rock-forming minerals (immobile) participating in the kinetic reactions was conserved through the solution of an ordinary differential equation (ODE).

Two numerical approaches are available in COMSOL to solve the nonlinear multiphysics problems: fully coupled and segregated. The Newton-Raphson iteration scheme is used in both of these approaches. In the fully coupled approach, various involved physics are coupled and solved at the same time. However, a fully coupled approach proves to be both memory- and time-intensive.

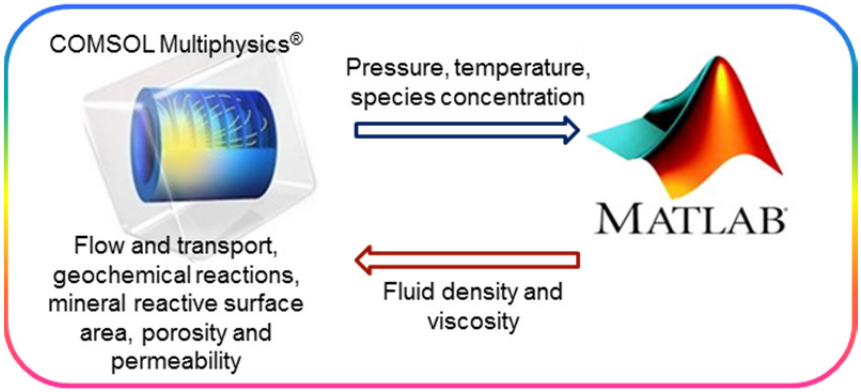

Fig. 2. Schematic of the coupling between COMSOL and MATLAB.

The segregated solution approach solves various involved physics problems sequentially by solving for various variables in sequence. The iteration process is continued until convergence is achieved. Iteration in the segregated approach takes less time than the iteration of the fully coupled approach. The segregated solver approach generally solves faster and proves to be more memory efficient than the fully coupled approach. Thus, in this study, a segregated technique that splits the solution process into sub-steps was used to solve the coupled reactive transport problem. A backward differentiation formula (BDF)-based time-dependent nonlinear solver was used with a Jacobian matrix that was updated every iteration. A damped version of Newton's method with a damping factor of 1 was used in all the involved sub-steps. The flow problems (pressure and velocity) were solved together in step 1. The transport of component species and the associated speciation were solved together in step 2. The temperature in the case of heat transport was solved in step 3, and finally, the mass conservation of kinetically controlled minerals was solved in step 4.

Various physical and geochemical interactions of leaking dissolved CO_2 with the porous media along the leakage pathway are included in the study. The geochemical reaction systems that may vary between the papers are considered in the reactive transport modelling. All the geochemical reactions, either equilibrium or mineral kinetics, are modelled as a function of temperature.

Storage of dissolved CO_2 in the pore spaces, its sorption on the mineral surfaces, and its conversion and consumption in aqueous and mineral reactions were analysed in the reactive transport modelling. Retention and related retardation of leaking dissolved CO_2 arising from considered physical and geochemical processes are investigated in the transport analysis.

3.2. Geochemical reaction system

Table 1 presents the overall geochemical system used in this study, which describes the water-rock interactions. First, eight reactions ((R0) to (R7)) are assumed to be fast and are thus modelled through the equilibrium assumption, whereas the last three reactions ((R8) to (R10)) are relatively slow mineral (calcite, dolomite and siderite) reactions and thus treated as kinetically controlled. The equilibrium between free-phase CO_2 and dissolved phase CO_2 was modelled by reaction (R0). The solubility model developed by Duan and Sun (2003), later improved by Duan et al. (2006), was used to model the solubility of CO_2 in the NaCl brine solution. The used model calculates the solubility of CO_2 in aqueous solutions containing Na^+, Cl^-, K^+, Ca^{2+}, Mg^{2+}, and SO_4^{2-}. This model covers wide ranges of pressure (from 0 to 2000 bar), temperature (from 273 to 533 K) and ionic strength (from 0 to 4.5 molal solutions). In their experimental study, Dilmore et al. (2008) have reported the reliability of the model of Duan and Sun (2003) to determine the solubility of CO_2 in the saline brine.

Reaction (R0) was only included in the batch geochemical modelling and was not involved in the subsequent reactive

Table 1. Equilibrium and mineral kinetic reactions considered in the study.

No.	Reactions
(R0)*	$CO_2 \leftrightarrow CO_{2aq}$
(R1)**	$H_2O + CO_{2aq} \leftrightarrow H^+ + HCO_3^-$
(R2)**	$H_2O \leftrightarrow H^+ + OH^-$
(R3)**	$HCO_3^- \leftrightarrow H^+ + CO_3^{2-}$
(R4)**	$Na^+ + HCO_3^- \leftrightarrow NaHCO_{3aq}$
(R5)**	$CaHCO_3^+ \leftrightarrow Ca^{2+} + HCO_3^-$
(R6)**	$MgHCO_3^+ \leftrightarrow Mg^{2+} + HCO_3^-$
(R7)**	$FeHCO_3^+ \leftrightarrow Fe^{2+} + HCO_3^-$
(R8)**	$CaCO_3 + H^+ \leftrightarrow Ca^{2+} + HCO_3^-$
(R9)**	$(CaMg)CO_3 + 2H^+ \leftrightarrow Ca^{2+} + Mg^{2+} + 2HCO_3^-$
(R10)**	$FeCO_3 + H^+ \leftrightarrow Fe^{2+} + HCO_3^-$

*Equilibrium reaction constant is based on Duan and Sun (2003) as modified by Duan et al. (2006).

**Equilibrium reaction constants are opted from "LLNL thermo database" (Delany and Lundeen, 1990) which is also used by The Geochemist's Workbench® as its default thermodynamic data.

transport modelling because the latter was performed for single-phase brine carrying dissolved CO_2.

3.3. Batch geochemical modelling

Batch geochemical modelling (BGM) simulates the equilibrium and mineral kinetic reactions without involving transport (Parkhurst and Appelo, 2013). In BGM, geochemical interactions between CO_2, pore water and rock minerals are performed until equilibrium. Batch reaction modelling was subdivided into (i) background BGM and (ii) CO_2 dissolution modelling. Background BGM was performed in the reservoir containing previously injected CO_2 as well as in the fractured caprock that was considered a leakage pathway (transport domain) lying above the reservoir. Background BGM provides the information of pressure (P), temperature (T) and geochemical conditions initially prevalent in the transport domain and was used as the initial conditions for the subsequent reactive transport modelling. BGM also provides the composition of the resident brine solution initially present in the reservoir before the placement of CO_2.

3.3.1. Background batch geochemical modelling

The initial pressure and temperature distribution in the transport domain was defined based on a hydrostatic pressure gradient of 1×10^4 Pa/m and a geothermal gradient of 0.03°C/m below the land surface (Pruess, 2008). The initial concentrations of dissolved species and related component species were found from the background BGM performed at a CO_2 partial pressure (P_{CO2}) of 1×10^3 Pa (Xu et al., 2005), adopting a 0.5 molar (M) solution of sodium chloride (NaCl) while including the fluid-mineral geochemical interactions.

The value of 0.5 M was adopted for the NaCl solution arbitrarily to represent the saline brine. The species chloride (Cl^-) was assumed to be conservative for its lack of participation in reactions

considered in this study (Table 1). The resident brine composition in the fractured clay-rich caprock (transport domain) obtained from the background BGM was in equilibrium with respect to the considered carbonate minerals, and thus, there was almost no reactivity between the fluid and the minerals. Thus, any reactivity in the subsequent reactive transport modelling can be attributed solely to the CO_2-saturated brine leaking from the reservoir.

3.3.2. CO_2 dissolution modelling

The composition of CO_2-saturated brine supposed to be leaking from the reservoir and that was required as a boundary condition for the reactive transport modelling was obtained by performing CO_2 dissolution modelling. In CO_2 dissolution modelling, the pressure of CO_2 was increased from a background pressure of 1×10^3 Pa to a value that represents the pressure conditions of the top boundary of the reservoir. Geochemical interactions between the considered carbonate minerals in the reservoir and the brine containing dissolved CO_2 were modelled until equilibrium conditions were reached with respect to the minerals.

3.4. Reactive transport modelling

3.4.1. Leakage of single-phase brine saturated with dissolved CO_2

For the fracture-matrix system, the solute transport in the fracture is governed by three transport processes, namely advection, dispersion and diffusion whereof diffusion is often acknowledged as the only transport process in the matrix (Novak, (1993, 1996); Steefel and Lichtner, (1998a, 1998b)). Hence, the mass exchange between the conducting principal pathway (fracture or fault zone) and the neighbouring less-permeable rock matrix takes place through matrix diffusion alone. In the first step, based on this concept, reactive transport modelling of the leaking dissolved CO_2 was performed by considering the diffusion alone as the the only transport process in the rock matrix (Paper I). However, in this thesis, the analysis was extended by including advection and dispersion in addition to diffusion as the transport processes in the rock matrix (Papers II and III). Reactive transport of leaking dissolved CO_2 was performed for a period of 500 years. For the considered time-scale, only the carbonate minerals calcite and dolomite, due to their fast kinetics, were considered for geochemical interactions with the brine carrying dissolved CO_2, whereas other minerals, present in the clay-rich caprock were considered non-reactive.

Conceptual transport model

A conceptual model used for the reactive transport of leaking CO_2-saturated brine, studied in Papers I, II and III, is presented in Fig. 3. A geological porous formation, with its upper boundary at a depth of 1040 m below the land surface, was assumed as a storage reservoir containing previously injected supercritical CO_2. The reservoir was assumed to be covered with overlying clay-rich low-permeable caprock containing a conducting fracture. The transport domain consists of a principal conducting pathway (fracture) on the left and the less-permeable rock matrix on the right. Symmetry

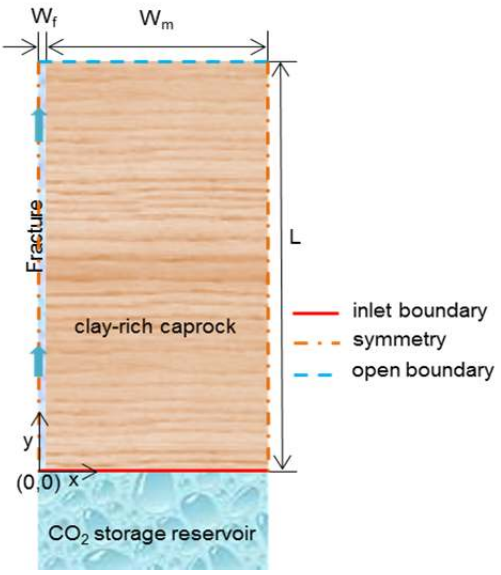

Fig. 3. Schematic of clay-rich caprock with a conducting pathway (fracture) overlying the CO_2 storage reservoir (not to scale).

was assumed along the left boundary in the y-direction (centre of the conducting pathway) and right side boundary of the rock matrix in the y-direction. Thus, no no-flow conditions were applied at the left side boundary (centre of the fracture) and the right side boundary of the rock matrix. CO_2-saturated brine leaking from the reservoir enters the transport domain through bottom inlet boundaries (y=0). After flowing through the fractured pathway, the fluid can leave the domain through the top boundaries (y=L). The mineralogical composition of clay-rich caprock was taken from Gherardi et al. (2007), with an initial porosity equal to 0.12 (Table 2).

3.4.2. Injection of dissolved CO_2 in the reservoir

In Paper IV, a porous carbonate reservoir (depth (D) = 250 m and width (W) = 500 m) was considered for the injection of dissolved CO_2 (Fig. 4). A 2D axisymmetric model was used in this reactive transport modelling. The upper boundary of the reservoir ($z = 0$) was considered to be 400 m below the land surface. CO_2-saturated

Table 2. Mineral composition of clay-rich caprock (Gherardi et al., 2007).

Minerals	Volume fraction in solid rock	Volume fraction in porous rock (12% porosity)
Calcite	0.29	0.255
Dolomite	0.04	0.035
Quartz	0.20	0.176
Illite	0.02	0.018
K-feldspar	0	0
Chlorite	0.06	0.053
Albite	0	0
Kaolinite	0.05	0.044
Na-smectite	0.15	0.132
Muscovite	0.19	0.1672

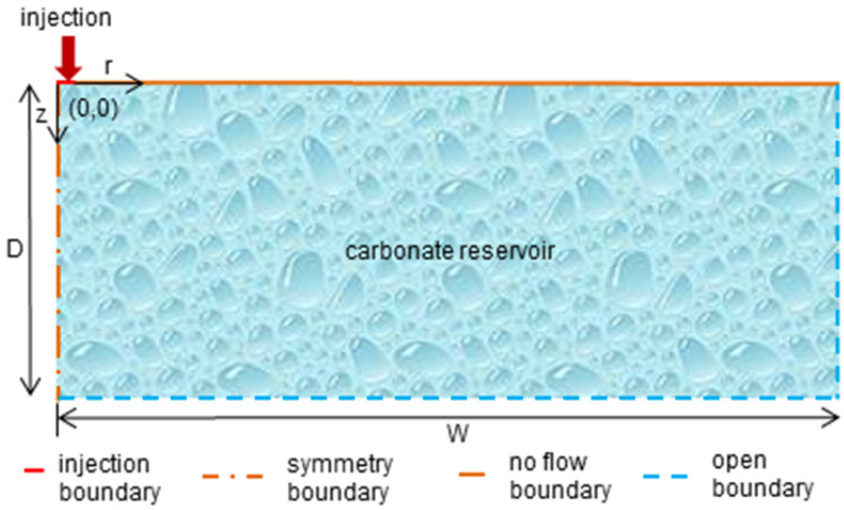

Fig. 3. Schematic of the carbonate reservoir considered for the storage of dissolved CO_2 (not to scale).

brine was injected through a 0.1 m wide inlet section at the left side ($0 \leq r \leq 0.1$) of the top boundary of the reservoir. A symmetry boundary with no-flow conditions exists across the left vertical boundary. Fluid can exit through the bottom and right vertical boundaries, whereas the top boundary was defined as a no-flow boundary. The reactive transport for the injection of dissolved CO_2 was performed for a period of 10 years.

3.4.3. Reactive transport and mass conservation of mobile species

The reactive transport system of mobile aqueous species was defined by the following equation written in terms of the species concentrations vector ($\mathbf{c}$) (COMSOL):

$$\mathbf{R_f}\theta\frac{\partial \mathbf{c}}{\partial t} + \left(\mathbf{1} - \mathbf{K_d}\rho_p\right)\mathbf{c}\frac{\partial \theta}{\partial t} - \nabla\cdot[(\mathbf{D_D} + \mathbf{D_e})\nabla\mathbf{c}] + \nabla\cdot(\mathbf{vc}) = \theta\mathbf{r_{kin}} \quad (1)$$

In this study, the reactive transport problem was formulated in terms of component species. Thus, in Eq. (1), a vector of aqueous species concentrations ($\mathbf{c}$) was replaced by a vector of concentrations of component species ($\mathbf{u}$):

$$\mathbf{R_f}\theta\frac{\partial \mathbf{u}}{\partial t} + \left(1 - \mathbf{K_d}\rho_p\right)\mathbf{u}\frac{\partial \theta}{\partial t} - \nabla\cdot[(\mathbf{D_D} + \mathbf{D_e})\nabla\mathbf{u}] + \nabla\cdot(\mathbf{vu}) = \theta\mathbf{r_{kin}} \quad (2)$$

where

$$\mathbf{R_f} = 1 + \frac{\rho_{bulk}}{\theta}\mathbf{K_d} \quad (3)$$

where $\nabla = (\partial/\partial x, \partial/\partial y)$ is the Nabla operator; $\mathbf{u}$ (x,y,t) is the vector of concentrations [mol/(kg water)] of the component species; $\mathbf{R_f}$ (x,y,t) is a diagonal matrix of retardation factors accounting for sorption of mobile component species with immobile phases; $\mathbf{K_d}$ (x,y,t) is a diagonal matrix where the diagonal elements include the sorption partition coefficients for involved component species [m^3/kg]; θ(x,y,t) is the spatially and temporally varying porosity; ρ_p (x,y,t) is the particle density [kg/m^3] of the rock formation; ρ_{bulk} (x,y,t) is the bulk density [kg/(m^3 bulk volume)] of the porous

media that changes with the porosity of the medium; $\mathbf{D_D}$ is the dispersion tensor [m^2/s]; $\mathbf{D_e}$ is the effective diffusion (diagonal) tensor [m^2/s] defined as a function of porosity of the medium; **v**(x,y,t) is Darcy's velocity vector [m/s] updated in space and time; and $\mathbf{r_{kin}}$(x,y,t) is the source/sink term defining the consumption or production of component species [mol/(s-kg water)]. In transport equations (2-3), **u** and $\mathbf{r_{kin}}$ are vectors of size equal to the number of component species, whereas $\mathbf{R_f}$ and $\mathbf{K_d}$ are matrices with rows and columns equal to the number of component species. The transport equations (2-3) are nonlinear partial differential equations in which the variables (θ, ρ_p, ρ_{bulk}), the matrices ($\mathbf{R_f}$ and $\mathbf{K_d}$) and the reaction term ($\mathbf{r_{kin}}$) are all nonlinear functions of the local concentrations of component species. The detailed methodology of calculating the medium porosity (θ), the particle density of rock (ρ_p) and the bulk density (ρ_{bulk}) of the medium is presented in Appendix A.

The transport equations (2-3) were written in terms of component species (*u*) that are defined as a linear combination of aqueous chemical species involved in the considered geochemical reaction system (Yeh and Tripathi, 1991; Steefel and Lasaga, 1994; Xu and Pruess, 2001). The mass conservation of aqueous species in the form of component species and the related source/sink term ($\mathbf{r_{kin}}$ (x,y,t)) involved in Eq. (2) were formulated following the methodology of Saaltink et al. (1998). A detailed formulation of aqueous species in terms of component species, derivation of the reaction term ($\mathbf{r_{kin}}$) and speciation was presented in the various papers for the considered reaction systems. The equilibrium reactions are defined through the law of mass action and result in algebraic equations. These algebraic equations were solved to compute the involved aqueous species as a function of transport component species (called speciation). Computation of the involved aqueous species is required because all the geochemical reactions are defined in terms of aqueous species. The transport system defined in terms of component species requires defining (i) the initial values of all aqueous species involved in the geochemical reactions and (ii) the initial and boundary values expressed in terms of the involved component species. The previously stored numerical solution from the BGM was used as the initial conditions in the subsequent reactive transport modelling. The transport problem can thus be solved by only specifying the boundary conditions.

3.4.4. Mass conservation of minerals

The minerals (considered as immobile species) undergoing kinetic reactions were mass conserved by means of the following ordinary differential equation (ODE):

$$\frac{\partial \mathbf{c_{m,bulk}}}{\partial t} = -\theta \rho_b \mathbf{r_m} \qquad (4)$$

where $\mathbf{c_{m,bulk}}$ is a vector representing the set of concentrations [mol/(m^3 bulk volume)] of individual mineral ($c_{m,bulk}$), ρ_b is the

density of brine/fluid, and θ is the medium porosity updated in time and space (Eq. 15). The initial values of mineral concentrations ($c_{m,bulk}$) were calculated from the initial volume fractions of the respective minerals in the porous media given in Table 2. The reaction term $\mathbf{r_m}$ is a vector representing the consumption or production [mol/(s-kg water)] of the individual mineral (r_m) that was defined in relation to its kinetically controlled dissolution or precipitation (Eq. 10).

3.4.5. Velocity field for the transport system

The velocity field in the transport equation (Eq. 2) was defined by the Brinkman equations. The Brinkman equations are a combination of the continuity equation and the momentum balance equation to define flow in the porous media:

$$\frac{\partial(\theta\rho_b)}{\partial t} + \nabla \cdot (\rho_b \mathbf{v}) = Q \tag{5}$$

$$\frac{\rho_b}{\theta}\left[\frac{\partial \mathbf{v}}{\partial t} + (\mathbf{v}\cdot\nabla)\frac{\mathbf{v}}{\theta}\right] = -\nabla p + \nabla \cdot \left[\frac{\mu_b}{\theta}\left\{(\nabla\mathbf{v} + (\nabla\mathbf{v})^T) - \frac{2}{3}(\nabla\cdot\mathbf{v})\mathbf{I}\right\}\right] - \left(\frac{\mu_b}{\kappa} + \frac{Q}{\theta^2}\right)\mathbf{v} + \mathbf{F} \tag{6}$$

where ρ_b is the density [kg/m^3] and μ_b is the dynamic viscosity [kg/(s-m)] of NaCl brine; p is the pressure [Pa]; κ is the permeability of the porous medium [m^2]; and Q is the mass source or sink, taken as zero in this study. The effect of gravity was included via the force term ($\boldsymbol{F} = -\rho_b \mathbf{g}$), where $\mathbf{g}$ is the gravitational acceleration vector (9.81 m/s^2). The Brinkman equations extend Darcy's law by introducing a term that accounts for the viscous effects in the momentum equation and defines both the pressure gradient and the flow velocity as independent vectors. Consistent with the Darcy law, the Brinkman equation represents the proportionality between the pressure gradient (first term on the right-hand side of Eq. (6)) and the viscous friction loss (represented by the third term on the right-hand side of Eq. (6)) but also include the inertia terms of the momentum equation. Popov et al. (2009) have reported the suitability of the Stokes-Brinkman equation for modelling the flow field in the porous media coupled to free flow regions, such as fractures, vugs, and caves. Gulbransen et al. (2010) have advocated for the Stokes-Brinkman equation compared to the Darcy-Stokes equation for modelling flow in the porous media and the free-flow regions where inertia effects are significant. Further, Brinkman equations are attractive numerically because they define the flow field in two regions (free flow and porous media) using a single system of equations, where the individual domain is represented by implicit parameters instead of the two-domain approach (Gulbranson et al., 2010). Several studies reports the use of Brinkman equations in COMSOL for modelling the flow in porous media (Sajjadi et al., 2014; Chabonan et al., 2015; Golfier et al., 2015; Basirat et al., 2015). The fluid density and viscosity were modelled as a function

of the temperature, pressure and concentration of dissolved species (CO_{2aq}, Na^+, and Cl^-). The code for formulation of fluid density and viscosity was developed based on the available published literature and was coupled with the transport problem. The detailed formulations for fluid density and viscosity are presented in Paper IV.

3.4.6. Heat transport

The following equation was used to model the heat transport by the migrating brine and its exchange with the porous media along the travel pathway (Bear and Bachmat, 1990; COMSOL):

$$\left(\rho C_p\right)_{eq}\frac{\partial T}{\partial t}+\rho_b C_{p,b}\mathbf{v}\cdot\nabla T=\nabla\cdot\left(k_{eq}\nabla T\right)+\nabla\cdot\left(k_d\nabla T\right) \quad (7)$$

where

$$\left(\rho C_p\right)_{eq}=(1-\theta)\rho_{pm}C_{p,pm}+\theta\rho_b C_{p,b} \quad (8)$$

and

$$k_{eq}=(1-\theta)k_{pm}+\theta k_b \quad (9)$$

where T is the temperature [K]; $\left(\rho C_p\right)_{eq}$ and k_{eq} represent the equivalent volumetric heat capacity [J/(m^3-K)] and thermal conductivity [W/(m-K)], respectively, of the solid-fluid system at constant pressure; ρ_{pm} and ρ_b represent the density [kg/m^3] of porous media and fluid respectively; $C_{p,pm}$ and $C_{p,b}$ are the heat capacity [J/(kg-K)] of porous media and fluid respectively; k_{pm} and k_b are the thermal conductivity [W/(m-K)] of porous media and fluid respectively; $k_d=\rho_b C_{p,b}D$ is the dispersive thermal conductivity; and $\mathbf{v}$ represents the Darcy's velocity defined by equations (5-6). Here the thermal dispersion (D) was defined as a function of thermal dispersivity which was taken equal to 1 m. The specific heat capacity of porous media was taken as 920 J/(kg-K), whereas its thermal conductivity was taken as 2.51 W/(m-K) (Pruess, 2005). The heat capacity ($C_{p,b}$) and thermal conductivity (k_b) of water carrying dissolved CO_2 were calculated on the mass averaged basis of water and dissolved CO_2, whereas the effects of other dissolved species were ignored (Papers III and IV).

3.4.7. Mineral kinetics

The reaction rate r_m in Eq. (4), which represents the consumption or production [mol/(s-kg water)] of the mineral as a result of its kinetic reaction, is defined as a function of the involved aqueous species and mineral reactive surface area (Lasaga et al., 1994):

$$r_m=k_m A_m\left[1-\frac{Q_m}{K_m}\right] \quad (10)$$

where k_m is the temperature-dependent kinetic rate constant of the mineral [mol/(s-m^2)], and A_m is the reactive surface area of the mineral [m^2/(kg water)] updated in time and space as a function of the updated mineral concentration and thus the volume fraction of

Table 3. Parameters for the various minerals involved in Eq. (11).

Mineral	k_{25} [mol/(s-m^2)]	E_a [KJ/mol]	Reference
calcite	1.60×10^{-9}	41.87	Svensson and Dreybrodt (1992)
dolomite	0.6×10^{-9}	41.87	assumed based on calcite
siderite	0.6×10^{-9}	41.87	assumed based on calcite

respective mineral. The ratio (Q_m/K_m) defines the saturation state of the mineral. The mineral dissolves in the solution if the saturation state of the solution with respect to the mineral is lower than unity, and it can precipitate if the saturation state of the solution becomes greater than unity. The term K_m is the equilibrium constant of the mineral defined as a function of temperature, whereas the term Q_m is called the ion activity product of the mineral, which is a function of the local concentrations of the involved aqueous species (e.g., for calcite H^+, Ca^{2+}, and HCO_3^-). The temperature dependent kinetic rate constant of the mineral (k_m) is defined by the following Arrhenius equation (Lasaga, 1984):

$$k_m = k_{25} exp\left[-\frac{E_a}{R}\left(\frac{1}{T}-\frac{1}{298.15}\right)\right] \quad (11)$$

where k_{25} is the reaction constant [mol/(s-m^2)] of the mineral at 25°C, E_a is the activation energy of the mineral [J/mol], R is the gas constant equal to 8.314 J/(mol-K), and T is the temperature [K]. The parameters used in Eq. (11) for various minerals considered in this study are presented in Table 3.

In Paper IV, to investigate the solution pH dependence of mineral kinetic reactions, the mineral kinetic rate constant was also defined by using the following relation (Palandri and Kharaka, 2004):

$$k_m = k_{25}^{H} exp\left[\frac{-E_a^{H}}{R}\left(\frac{1}{T}-\frac{1}{298.15}\right)\right] a_H^{n_H} + k_{25}^{nu} exp\left[\frac{-E_a^{nu}}{R}\left(\frac{1}{T}-\frac{1}{298.15}\right)\right] + k_{25}^{OH} exp\left[\frac{-E_a^{OH}}{R}\left(\frac{1}{T}-\frac{1}{298.15}\right)\right] a_H^{n_{OH}} \quad (12)$$

The above relation considers three mechanisms (acid, neutral and base) for computing the mineral kinetic rate constant. In Eq. (12), the superscripts H, nu, and OH represent the acid, neutral and base mechanisms, respectively; a_H represents the activity of H^+; and the superscripts n_H and n_{OH} are the reaction order with respect to the activity of H^+. The parameters for Eq. (12) are presented in Table 4. All three mechanisms (acid, neutral and base) are involved in the rate constant for the minerals calcite and dolomite (Palandri and Kharaka, 2004), whereas the rate constant of siderite is defined by the acid and neutral mechanisms (Xu et al., 2007).

3.4.8. Computation of the activity coefficients of aqueous species

The chemical species appear in the geochemical reactions as their activity and not as their concentration. The activity of aqueous chemical species (a) is the product of the activity coefficient (γ)

Table 4. Parameters for the various minerals involved in Eq. (12).

Mineral	Acid mechanism			Neutral mechanism		Base mechanism		
	k_{25}^{H} [mol/(s-m^2)]	n_{H}	E_a^H [KJ/mol]	k_{25}^{nu} [mol/(s-m^2)]	E_a^{nu} [KJ/mol]	k_{25}^{OH} [mol/(s-m^2)]	n_{OH}	E_a^{OH} [KJ/mol]
calcite*	0.50	1	14.3	1.55×10^{-6}	23.5	3.31×10^{-4}	1	35.4
dolomite*	1.74×10^{-4}	0.5	56.7	2.51×10^{-9}	95.3	4.27×10^{-6}	0.5	45.7
siderite**	6.46×10^{-4}	0.5	36.1	1.26×10^{-9}	62.76	0	--	--

* Palandri and Kharaka, 2004; ** Xu et al., 2007

and the species concentration (c) related through the following relation:

$$a_i = \gamma_i \frac{c_i}{c_0} \tag{13}$$

where c_0 is the standard concentration [1 mol/(kg water)]. The species activity coefficient is defined as a function of the species concentration in the solution. The activity coefficient of dissolved CO_2 was based on the model presented by Duan and Sun (2003). The activity coefficients of electrically charged species were obtained from the extended Bebye-Hückel function (B-dot model), whereas the activity coefficients of electrically neutral species were calculated using the relationship presented by Bethke (2008) (Paper I).

3.4.9. Mineral reactive surface area

Mineral dissolution or precipitation through mineral kinetic reactions not only cause variations in the porosity and permeability of the medium but also result in variations in the reactive surface area of the minerals involved in reactions. Variations in the mass of minerals [mol/(m^3 bulk volume)] result from their geochemical interactions with the fluid, expressed by Eq. (4), that in turn change the reactive surface area [m^2/(kg water)] of the minerals. The temporally and spatially varying reactive surface area of the mineral (A_m) was computed using the following relation:

$$A_m = 0.1\,(\frac{A_g}{\theta \rho_b V_g})\,\left(MV_m c_{m,bulk}\right) \tag{14}$$

where A_g and V_g represent the physical surface area and volume of the mineral grain, respectively, assuming the grain is spherical with a radius of 1.65×10^{-5} m; MV_m is the molar volume of the mineral; ρ_b is the density of brine fluid; and $c_{m,bulk}$ is the mineral concentration updated in time and space through Eq. (4). Eq. (14) also accounts for the effects of fluid density (ρ_b) that may vary in time and space. A multiplication factor of 0.1 represents the mineral's reactive surface area as a fraction of its corresponding geometrical surface area (Johnson et al., 2004). The detailed methodology of computing the initial and varying reactive surface area (A_m) of minerals is presented in Appendix A.

3.4.10. Medium porosity

Minerals can either dissolve or precipitate in the computational domain over a period of time, causing changes in the

concentrations of minerals through Eq. (4). This causes changes in the mineral volume fraction and thus the porosity of the porous media. These space- and time-dependent variations in the porosity of the porous media were modelled in relation to the updated volume fraction of minerals of the porous media using the following relation:

$$\theta = 1 - VF_{rock,p} \tag{15}$$

where $VF_{rock,p} = \sum VF_{m,p}$ is the sum of the volume fractions of all the minerals composing the porous rock; and $VF_{m,p} = V_{m,p}/V_{rock,p}$ [-] is the volume fraction of the mineral, expressed as the ratio of the mineral volume to the total volume of the porous medium. The detailed methodology of calculating the medium porosity (θ) from the updated volume fraction of minerals forming the porous rock medium is also presented in Appendix A. The medium porosity was not allowed to reach unity by setting a minimum threshold concentration value for all the involved minerals of 1×10^{-7} [mol/(m^3 bulk volume)] in Eq. (4). Porosity of the medium was also maintained at a minimum value of 1×10^{-3} by stopping precipitation of minerals whenever the porosity falls to this minimum value in the domain.

3.4.11. Medium permeability

The initial permeability (κ_0) of the porous medium was found from the Kozeny-Carman relation as a function of the initial porosity (θ_0) and the mineral composition of the porous media (Bear and Cheng, 2010):

$$\kappa_0 = C\frac{\theta_0^3}{(1-\theta_0)^2\left(A_{rock,SSAV}\right)^2} \tag{16}$$

where C is a coefficient equal to 0.2 and $A_{rock,SSAV}$ is the initial specific surface area of the solid rock per unit volume of the solid rock [m^2/m^3], which depends on the initial mineral composition of the porous media (Bear & Cheng, 2010). The expressions for calculating $A_{rock,SSAV}$ are also presented in Appendix A. The medium permeability was updated in time and space as a function of the medium porosity using the following Kozeny-Carman relation (Lai et al., 2014):

$$\kappa = \kappa_0\frac{(1-\theta_0)^2\theta^3}{(1-\theta)^2\theta_0^3} \tag{17}$$

3.4.12. Sorption of mobile species on mineral surfaces

Aqueous species may undergo a sorption process on the surfaces of the minerals in the porous media. The sorption process may fix the quantities of aqueous species in the sorbed state and may cause the transport retardation of species. The effect of sorption appears in the transport equations (2-3) through the retardation factor ($\mathbf{R}_f$). A linear K_d model was used to study the sorption of aqueous species on rock surfaces defined through the following equilibrium

reaction (Freeze and Cherry, 1979; Bodin et al., 2003; Bear and Cheng, 2010):

$$K_{d,ii} = \left.\frac{c_{s,i}}{c_i}\right|_{eq} \quad (18)$$

where $c_{s,i}$ is the *i*-th component of the vector of concentrations of aqueous species sorbed on the surface of a solid phase (immobile minerals) that is expressed as the species concentration per unit mass of a solid [mol/kg], c_i is the *i*-th component of the vector of concentrations of species in the fluid phase [mol/m^3], $K_{d,ii}$ is the *i*-th diagonal component of the partition matrix $\mathbf{K_d}$, and thus $\mathbf{K_d}$ has the units of m^3/kg. However, in this study, the sorption process was modelled using a constant value of the partition coefficient K_d for all species.

Various minerals have shown the ability to adsorb CO_2 on their surfaces (Santschi and Rossi, 2006; Fujii et al., 2010; Tabrizy et al., 2013; Heller and Zoback, 2014). Calcite presents a partition coefficient of 6.6×10^{-2} m^3/kg for CO_2 (Santschi and Rossi, 2006). In their experimental study, Fujii et al. (2010) have observed the adsorption of CO_2 on various rocks and minerals at temperature and pressure conditions relevant to CO_2 geological storage. In the experimental study of Heller and Zoback (2014), the clay sample "Eagle Ford" consisting of mainly calcite (80%) has shown a partition coefficient of 7.39×10^{-4} m^3/kg for CO_2 at a pressure of 10.5 MPa (relevant pressure conditions in the CO_{2aq} leakage modelling in this study). The deduced values of the partition coefficient for various clay samples from the study of Heller and Zoback (2014) are presented in Table 5.

In this study, three different values ($7.50\text{x}10^{-4}$, $2.50\text{x}10^{-4}$, and $8.33\text{x}10^{-5}$ m^3/kg) of the partition coefficient were used that are lower than the values reported by Santschi and Rossi (2006) and by Heller and Zoback (2014). In addition, the same value of the

Table 5. Sorption partition coefficient (K_d) for CO_2 for various clay samples (Heller and Zoback, 2014).

Clay sample	Barnett 31	Marcellus	Montney	Eagle Ford 127
Calcite content (%)	0	1	8.1	80
Clay content (%)	37.4	52	24.1	5
K_d [m^3/kg] value at 10.5 MPa	3.18×10^{-3}	1.54×10^{-3}	3.33×10^{-3}	7.39×10^{-4}
K_d [m^3/kg] value at 15.5 MPa	3.45×10^{-3}	1.62×10^{-3}	3.60×10^{-3}	7.93×10^{-4}

Table 6. Parameters for equations (19-20) computed at three different pressure and temperature conditions.

Pressure and Temperature	Viscosity of water (μ_0) [kg(m-s)]	Viscosity of brine (μ_b) [kg/(m-s)]	Diffusion coefficient of CO_2 in water (D_0) [m^2/s]	Diffusion coefficient of CO_2 in brine (D_b) [m^2/s]
41×10^5 Pa and 27°C	8.51×10^{-4}	8.90×10^{-4}	2.10×10^{-9}	2.02×10^{-9}
105×10^5 Pa and 45°C	5.96×10^{-4}	6.27×10^{-4}	3.19×10^{-9}	3.05×10^{-9}
151×10^5 Pa and 60°C	4.69×10^{-4}	4.94×10^{-4}	4.25×10^{-9}	4.05×10^{-9}

partition coefficient was used for all the aqueous species due to the large uncertainty in the sorption properties and the involved complex geochemical interactions.

3.4.13. Diffusion of species in porous media

The species diffusion in the porous media was defined as an effective diffusion ($\mathbf{D_e}$) that is related to the medium porosity ($\mathbf{D_e} = \theta D_b \mathbf{I}$), where $\mathbf{I}$ is the identity tensor. The diffusion coefficient for dissolved CO_2 in brine fluid (D_b) was computed from its diffusion coefficient in water (D_0) as follows (Al-Rawajfeh, 2004; Hassanzadeh et al., 2008):

$$D_b = 10^{[-0.87 \log(\frac{\mu_b}{\mu_0})]} D_0 \quad (19)$$

where μ_0 and μ_b represent the viscosities of water and brine (H_2O+NaCl+CO_2), respectively. The viscosity of pure water and brine fluid was computed from the model presented by Mao and Duan (2009) (Paper I). The diffusion coefficient of dissolved CO_2 in water was calculated from the relation (Al-Rawajfeh, 2004):

$$D_0 = 10^{(-4.1764 + \frac{712.52}{T} - \frac{2.5907 \times 10^5}{T^2})} \quad (20)$$

The viscosity of water and brine and the diffusion coefficient of CO_2 in water and brine were computed from equations (19-20) at various pressure and temperature conditions as presented in Table 6. The computed value of the diffusion coefficient (D_b) for dissolved CO_2 was taken as the diffusion coefficient for all the mobile species (Gherardi et al., 2007).

3.4.14. Methodology for calculating the mass conversion of CO_2 in geochemical reactions

The mass consumption of CO_{2aq} in geochemical reactions in each reactive transport scenario was computed by comparing CO_{2aq} mass balances with the corresponding mass transport scenario without involving those reactions presented in Table 1. Thus, in this study, in addition to the reactive transport scenarios, an equal number of mass transport scenarios were also performed for computation of the mass consumption of CO_{2aq} in each reactive transport scenario. In addition to presenting the mass consumption in terms of cumulative quantities (m_{con}), it was also presented as a percentage ($\% m_{con} = \frac{m_{con}}{m_{in}}$) of cumulative quantities that entered the domain (m_{in}) from the reservoir over the period of time.

3.5. Detailed description of various transport processes analysed in the various papers

Table 7 provides the summary of various transport processes studied in Papers I through III. Sections 3.5.1 – 3.5.4 describe the details of various transport processes analysed in the individual papers.

Table 7. Summary of transport processes modelled in Papers I through III.

Paper	Processes in the fracture	Processes in the rock matrix	Parameters investigated in the sensitivity analysis
I	advection, dispersion, diffusion and aqueous phase reactions	diffusion, sorption, aqueous phase reactions plus kinetic reaction of calcite	velocity in fracture, sorption partition coefficient, temperature and diffusion coefficient
II	advection, dispersion, diffusion, sorption and aqueous phase reactions plus the kinetic reaction of calcite	advection, dispersion, diffusion, sorption and aqueous phase reactions plus the kinetic reaction of calcite	velocity and dispersion
III	advection, dispersion, diffusion, sorption and aqueous phase reactions plus the kinetic reaction of calcite and dolomite	advection, dispersion, diffusion, sorption and aqueous phase reactions plus the kinetic reaction of calcite and dolomite	geochemical system and heat transport (temperature)

3.5.1. Paper I

In this paper, a bedrock fracture was considered as the principal conducting pathway with porosity of 100% and without any infill material. The adjacent less-permeable rock matrix was assumed as a stagnant zone. Advection, dispersion and diffusion were considered as the transport processes in the conducting fracture, whereas diffusion was the only transport process considered in the neighbouring rock matrix for mass exchange between the fracture and the matrix. The considered transport domain was 20 m long, consisting of a 1 mm wide fracture on the left and a 10 m wide rock matrix on the right (Fig. 3). In the base-case scenarios (Table 8), a constant vertical fluid velocity in the fracture was taken as 3.171×10^{-7} m/s (nearly 10 m/year). The longitudinal dispersion coefficient (D_L) in the fracture was defined using Taylor-Aris dispersion:

$$D_D = D_L = D_b + \frac{2}{105 D_b} v^2 W_f^2 \qquad (21)$$

where v and W_f represent the vertical mean velocity in the fracture and the half-width of the fracture spacing, respectively. The mean velocity is generally expressed as v/θ, where v is the Darcy velocity, but the porosity was 100% in the considered fracture. Both diffusion and dispersion processes are embedded in Eq. (21) for the case of fracture.

The geochemical system considered in this paper includes four equilibrium reactions and one kinetic reaction of mineral calcite ((R1)-(R4) and (R8) presented in Table 1). For the considered reaction system, a total of four (4) component species result from eight (8) aqueous species that were involved in the geochemical reactions. Thus, for the considered geochemical system in Paper I, the transport equations (2–3) involve four component species. Aqueous-phase equilibrium reactions were considered in both the fracture and the rock matrix, whereas the calcite kinetic reaction was only considered in the rock matrix.

Table 8. Various base-case transport scenarios modelled for 500 years.

Scenarios	Processes accounted for
1	No interaction between the fracture and matrix
2	Molecular diffusion between the fracture and matrix, without sorption and calcite reaction in the matrix
3	Molecular diffusion between the fracture and matrix, with sorption and without calcite reaction in the matrix
4	Molecular diffusion between the fracture and matrix, without sorption and with calcite reaction in the matrix
5	Molecular diffusion between the fracture and matrix, with sorption and calcite reaction in the matrix

Table 9. Sensitivity analysis performed for various parameters for 500 years.

Sub-scenarios	Velocity [m/s] in the fracture	Distribution coefficient [m^3/kg]	Pressure and temperature
3.1	$3.17x10^{-8}$	$2.50x10^{-4}$	105×10^5 Pa and 45°C
3.2	$6.34x10^{-7}$	$2.50x10^{-4}$	105×10^5 Pa and 45°C
3.3	$3.17x10^{-7}$	$7.50x10^{-4}$	105×10^5 Pa and 45°C
3.4	$3.17x10^{-7}$	$8.33x10^{-5}$	105×10^5 Pa and 45°C
5.1	$3.17x10^{-8}$	$2.50x10^{-4}$	105×10^5 Pa and 45°C
5.2	$6.34x10^{-7}$	$2.50x10^{-4}$	105×10^5 Pa and 45°C
5.3	$3.17x10^{-7}$	$7.50x10^{-4}$	105×10^5 Pa and 45°C
5.4	$3.17x10^{-7}$	$8.33x10^{-5}$	105×10^5 Pa and 45°C
3a	$3.17x10^{-7}$	$2.50x10^{-4}$	155×10^5 Pa and 60°C
5a	$3.17x10^{-7}$	$2.50x10^{-4}$	155×10^5 Pa and 60°C
3b	$3.17x10^{-7}$	$2.50x10^{-4}$	155×10^5 Pa and 60°C
5b	$3.17x10^{-7}$	$2.50x10^{-4}$	155×10^5 Pa and 60°C

To evaluate the significance of the physical and geochemical transport processes on the transport of leaking dissolved CO_2, various scenarios were modelled for a period of 500 years (Table 8). Mass transport without involving any of the geochemical reactions (those presented in Table 1) was analysed in the different mass transport scenarios 1, 2 and 3, whereas reactive transport was modelled in scenarios 4 and 5. Scenario 1 considers the fluid flow only in the fracture without any interaction between the fracture and the matrix. Sorption was included in scenarios 4 and 5 by using a partition coefficient of $2.50x10^{-4}$ m^3/kg. We considered scenarios 1 to 5 as the base-case scenarios. Sensitivity analysis was also performed to understand the effects of various parameters (velocity in the fracture, sorption partition coefficient, pressure and temperature) on the consumption and retention of dissolved CO_2 along the leakage pathway (Table 9). Base-case scenarios 3 and 5 were used also for the sensitivity analysis. In the sensitivity analysis, mass transport without reactions was modelled in scenarios 3.1, 3.2, 3.3, 3.4 and 3a, whereas the corresponding reactive transport was modelled in scenarios 5.1, 5.2, 5.3, 5.4 and 5a.

3.5.2. Paper II

In this paper, a conducting fracture was assumed as partially filled with minerals (Wealthall et al., 2001; Laubach et al., 2010; Wu et al., 2010; Liu et al., 2013). The porosity of the conducting fracture was taken as 0.6. The considered transport domain was 100 m long, consisting of a 1 mm wide fracture on the left and a 50 m wide rock matrix on the right (Fig. 3). The analysis performed in Paper I was extended by including advection and dispersion in addition to diffusion as the transport processes in the rock matrix. Moreover, sorption and mineral reactions were also included in the fracture in addition to the rock matrix. Brinkman equations (5-6) were used to model the fluid flow as a function of variations in medium porosity and permeability resulting from mineral dissolution and precipitation. The geochemical system was similar to that used in Paper I, i.e., reactions (R1)-(R4) and (R8). The sorption process was considered in scenarios 3 and 4.

The base-case reactive transport scenarios 1 to 4 were performed to investigate the role of advection and dispersion compared to diffusion alone in the rock matrix on the fate of leaking dissolved CO_2 (Table 10). We use the terms "diffusive transport" for the transport that consider diffusion alone in the rock matrix and "advection dominated transport" that includes advection, dispersion and diffusion in the rock matrix. In diffusive transport scenarios 1 and 3, diffusion alone exists in the rock matrix, whereas in advective transport scenarios 2 and 4, advection and dispersion were also included in addition to diffusion in the rock matrix. Because the pressure difference between the bottom and top boundaries defines the vertical velocity along the transport pathway, in these base-case scenarios, to attain a vertical velocity of nearly 10 m/year in the conducting fracture, an excess pressure of 71.625 Pa was applied in addition to the prevailing hydrostatic pressure at the bottom inlet boundary. The used velocities are representative of flow velocities in deep sedimentary basins (Bachu et al., 1994). In the sensitivity analysis, scenarios 5 to 8 were performed to analyse the role of fluid velocity and dispersivity.

3.5.3. Paper III

In this paper, the role of geochemical reactions and temperature (including heat transport by migrating brine) on the leaking

Table 10. Various reactive transport scenarios performed in the base-case and the sensitivity analysis for a period of 500 years.

Reactive transport scenario	Partition coefficient [m^3/kg]	Initial velocity [m/year] in the fracture	Longitudinal dispersivity [m] in the fracture	Longitudinal dispersivity [m] in the matrix	Excess pressure [Pa] at the bottom
1	0	10	10	0	71.625
2	0	10	10	10	71.625
3	2.5×10^{-4}	10	10	0	71.625
4	2.5×10^{-4}	10	10	10	71.625
5	0	5	10	10	20.750
6	0	15	10	10	122.50
7	0	10	20	20	71.625
8	0	10	30	30	71.625

dissolved CO_2 was investigated (Table 11). Compared to Papers I and II, a relatively longer travel pathway was considered in Paper III. The transport domain was 250 m long, consisting of a conducting fracture (1 mm wide) on the left and a rock matrix (125 m wide) on the right (Fig. 3). Same as in Paper II, an initial porosity of fracture was taken equal to 0.6.

Scenario 1 represents the geochemical system that was studied in Papers I and II. Thus, the geochemical system considered in scenario 1 consists of four equilibrium reactions plus one mineral kinetic reaction ((R1)-R4) and (R8)) and here is termed as a "simplified geochemical system." Compared to scenario 1, scenario 2 considers an additional equilibrium reaction (R5). The rest of the scenarios, 3 through 6, consider two additional equilibrium reactions plus one kinetic reaction of the mineral dolomite ((R5), (R6) and (R9) presented in Table 1) compared to scenario 1. Thus, the reaction system in scenarios 3 through 6 consists of six equilibrium reactions ((R1)-(R6)) plus two mineral kinetic reactions ((R8)-(R9)) and here is termed as an "extended geochemical system." Scenarios 1 through 3 were performed considering a constant temperature (T constant) of 27°C in the travel pathway. A vertical temperature gradient (T gradient) was considered in scenario 4, whereas heat transport (T flow) by leaking brine was included in scenarios 5 and 6. Sorption process was considered only in scenario 6 by using a sorption partition coefficient of 8.33×10^{-5} m^3/kg (Santschi and Rossi, 2006; Heller and Zoback, 2014; Ahmad et al, 2015).

An excess pressure of 500 Pa, in addition to prevailing hydrostatic pressure, was applied at bottom inlet boundary for a vertical velocity of nearly 20 m/year in the fracture. Dispersion was defined using longitudinal and transverse dispersivity of 25 m and 1 m, respectively, in both the fracture and the rock matrix. The density and viscosity of NaCl brine were defined at constant values of P (105×10^5 Pa) and T (45°C) for fluid velocity independent of P and T variations for a fair comparison of results between the scenarios.

3.5.4. Paper IV

CO_2 dissolved in brine was injected in the subsurface carbonate reservoir for a period of 10 years. Physical and geochemical interactions between the injected brine containing dissolved CO_2, and the carbonate minerals (calcite, dolomite and siderite) were investigated in the reactive transport modelling. The geochemical

Table 11. Various reactive transport scenarios performed for 500 years.

Scenario	Minerals considered	Reaction system	Temperature along flow pathway	Partition coefficient [m^3/kg]
1	calcite	(R1)-(R4), (R8)	Constant	0
2	calcite	(R1)-(R5), (R8)	Constant	0
3	calcite, dolomite	(R1)-(R6), (R8)	Constant	0
4	calcite, dolomite	(R1)-(R6), (R8)-(R9)	Gradient	0
5	calcite, dolomite	(R1)-(R6), (R8)-(R9)	Flow	0
6	calcite, dolomite	(R1)-(R6), (R8)-(R9)	Flow	8.33×10^{-5}

reaction system comprises seven equilibrium and three mineral kinetic reactions ((R1)-(R10) presented in Table 1). The initial volume fractions of 0.30, 0.44 and 5.21×10^{-3} for calcite, dolomite and siderite, respectively, were calculated for an assumed initial reservoir porosity of 0.25 and from the mass fractions of these minerals in the carbonate reservoir reported by Zerai et al. (2006) (Table 12). For the considered initial reservoir porosity of 0.25, we calculated the initial permeability of the reservoir as 6.46×10^{-13} m^2.

The brine can be pumped out of the targeted carbonate reservoir and injected back carrying dissolved CO_2 (Eke at al., 2011; CO2-DISSOLVED Project). In the injection well, CO_2 is transported in a separate pipe parallel to the one injecting the brine, and the two streams are mixed before their injection in the reservoir (Alfredsson et al., 2013; Pool et al., 2013; Gislason and Oelkers, 2014). The resulting CO_2-saturated brine was injected in the reservoir through a 0.1 m wide inlet section at the top of the reservoir with a velocity of 0.5 m/s, which corresponds to nearly 16 kg/s of brine (nearly 14.5 mol/s or 0.64 kg/s of dissolved CO_2) (Fig. 4).

Various reactive transport scenarios were performed for a period of 10 years to analyse the mass of injected CO_{2aq} stored in aqueous and adsorbed states and consumed in geochemical reactions in the reservoir (Table 13). Scenarios 1 through 5 and 8 were performed for a considered constant temperature of 27°C in the reservoir (T constant). Sorption was only considered in scenario 2 using a partition coefficient of $2.50\text{x}10^{-4}$ m^3/kg. The role of dispersivity, temperature and minerals kinetic rate constant was investigated in the sensitivity analysis. The role of dispersivity was analysed in scenarios 3 through 5, whereas scenarios 6 and 7 analyse the role of temperature. Scenarios 6 and 7 include the cooling transfer (T flow) by the relatively cooler CO_2-saturated brine injected in the reservoir. In scenario 8, the dependence of mineral kinetic

Table 12. Mineral composition of the carbonate reservoir (Zerai et al., 2006).

Mineral	Weight (%)	Volume fraction in solid mass	Volume fraction for a porosity of 25%
calcite	39	0.40	0.30
dolomite	60	0.59	0.44
siderite	1	6.95×10^{-3}	5.21×10^{-3}

Table 13. Various reactive transport scenarios performed for 10 years.

Scenarios	Injection temperature [°C]	Temperature conditions in the reservoir	Mineral kinetic rate constant	Sorption	Dispersivity [m]	
					D_L	D_T
1	27	constant	Eq. (11)	No	50	5
2	27	constant	Eq. (11)	Yes	50	5
3	27	constant	Eq. (11)	No	10	1
4	27	constant	Eq. (11)	No	100	10
5	27	constant	Eq. (11)	No	100	50
6	17	flow	Eq. (11)	No	100	50
7	7	flow	Eq. (11)	No	100	50
8	27	constant	Eq. (12)	No	100	50

reactions on the pH of the brine solution was analysed. In this scenario, the mineral kinetic rate constants were defined by using Eq. (12), which takes into account the effects of the solution pH. The density and viscosity of the brine fluid were based on the vertical gradients of P and T in the reservoir and also take into account the effects of dissolved species (Na^+, Cl^-, and CO_{2aq}) (Paper IV).

4. RESULTS AND DISCUSSION

4.1. Batch geochemical modelling

4.1.1. Papers I and II

The background BGM provided the composition of equilibrated resident brine in the transport domain. Table 14 presents the composition of resident brine at a pressure of 1×10^3 Pa and at temperatures of 45°C (column 2) and 60°C (column 3). The equilibrated resident brine prevailing in the transport domain attained the pH values of 7.264 and 7.261 at 45°C and 60°C,

Table 14. Species concentrations from the background BGM at a pressure of 1×10^3 Pa and temperature values of 45°C (column 2) and 60°C (column 3).

Pressure and temperature	1×10^3 Pa and 45°C	1×10^3 Pa and 60°C
Aqueous species	Concentration [mol/(kg water)]	Concentration [mol/(kg water)]
HCO_3^-	3.33×10^{-3}	2.66×10^{-3}
Na^+	5.00×10^{-1}	5.00×10^{-1}
Ca^{2+}	2.01×10^{-3}	1.55×10^{-3}
CO_{2aq}	1.98×10^{-4}	1.54×10^{-4}
H^+	5.44×10^{-8}	5.49×10^{-8}
OH^-	1.29×10^{-6}	3.33×10^{-6}
CO_3^{2-}	1.43×10^{-5}	1.29×10^{-5}
$NaHCO_{3aq}$	6.63×10^{-4}	4.12×10^{-4}

Table 15. Initial (sub-index 0) and boundary values (sub-index bc) used in reactive transport at two different pressure and temperature conditions.

Pressure and temperature	105×10^5 Pa and 45°C	155×10^5 Pa and 60°C
Component species	concentration [mol/(kg water)]	concentration [mol/(kg water)]
$u_{\mathrm{HCO}_{3,0}}$	4.02×10^{-3}	3.10×10^{-3}
u_{Na_0}	5.00×10^{-1}	5.00×10^{-1}
u_{Ca_0}	2.01×10^{-3}	1.55×10^{-3}
$u_{\mathrm{CO}_{2,0}}$	1.82×10^{-4}	1.38×10^{-4}
$u_{\mathrm{HCO}_{3,\mathrm{bc}}}$	7.17×10^{-2}	5.95×10^{-2}
$u_{\mathrm{Na}_{\mathrm{bc}}}$	5.00×10^{-1}	5.00×10^{-1}
$u_{\mathrm{Ca}_{\mathrm{bc}}}$	3.58×10^{-2}	2.97×10^{-2}
$u_{\mathrm{CO}_{2,\mathrm{bc}}}$	1.08	1.06

respectively. These equilibrated geochemical conditions were also expressed in terms of component species to define the initial values required for the subsequent reactive transport modelling (sub-index 0 in Table 15). The boundary values for the reactive transport modelling were obtained from the CO_2 dissolution modelling at two different pressure and temperature conditions (sub-index bc in Table 15). The pH values of CO_2- saturated brine resulting from the dissolution of CO_2 in the reservoir decreased to 4.78 (at 45°C and 105×10^5 Pa) and 4.71 (at 60°C and 155×10^5 Pa). These two pressure and temperature conditions used in the BGM correspond to two different pressure and temperature conditions used in the reactive transport modelling in Paper I. Although the geochemical system used in Paper II was the same used in Paper I, the simulations were performed only at 45°C and 105×10^5 Pa in this paper. Thus, the relevant geochemical conditions for Paper II are those in column 2 of Table 14 and Table 15.

4.1.2. Paper III

Background BGM in the transport domain was performed for

Table 16. Initial brine composition in the transport domain from background BGM for scenario 4.

Species	Concentration [mol/(kg water)] at the bottom boundary of the transport domain	Concentration [mol/(kg water)] at the top boundary of the transport domain
CO_{2aq}	1.98×10^{-4}	2.29×10^{-4}
HCO_3^-	3.42×10^{-3}	3.87×10^{-3}
Na^+	4.99×10^{-1}	4.99×10^{-1}
Ca^{2+}	1.90×10^{-3}	2.18×10^{-3}
Mg^{2+}	1.48×10^{-4}	1.85×10^{-4}
$CaHCO_3^+$	3.35×10^{-5}	4.03×10^{-5}
$MgHCO_3^+$	1.92×10^{-6}	2.57×10^{-6}
H^+	5.29×10^{-8}	5.34×10^{-8}
OH^-	1.33×10^{-6}	8.16×10^{-7}
CO_3^-	1.51×10^{-5}	1.58×10^{-5}
$NaHCO_{3aq}$	6.82×10^{-4}	8.73×10^{-4}

Table 17. Composition of the CO_2-saturated brine supposed to leak from the reservoir in scenario 3.

Species	Concentration [mol/(kg water)]	Species	Concentration [mol/(kg water)]
CO_{2aq}	1.08	OH^-	4.58×10^{-9}
HCO_3^-	6.50×10^{-2}	CO_3^-	1.03×10^{-6}
Na^+	4.88×10^{-1}	$NaHCO_{3aq}$	1.22×10^{-2}
Ca^{2+}	3.09×10^{-2}	$u_{\mathrm{HCO_{3,bc}}}$	8.76×10^{-2}
Mg^{2+}	2.36×10^{-3}	$u_{\mathrm{Na_{bc}}}$	5.00×10^{-1}
$CaHCO_3^+$	9.93×10^{-3}	$u_{\mathrm{Ca_{bc}}}$	4.09×10^{-2}
$MgHCO_3^+$	5.69×10^{-4}	$u_{\mathrm{Mg_{bc}}}$	2.93×10^{-3}
H^+	1.55×10^{-5}	$u_{\mathrm{CO_{2,bc}}}$	1.08

scenarios 1 through 5 (presented in Table 11) in relation to the considered reactive transport modelling scenarios. This resulted in different initial geochemical conditions in the transport domain in each scenario. Similarly, CO_2 dissolution modelling in the reservoir was performed for scenarios 1 through 3 for the reactions considered in the respective scenarios until the solution was saturated with respect to the minerals.

The composition of brine initially present in the transport domain for scenario 4, which considered the vertical temperature gradient in the transport domain, is presented in Table 16. The brine composition at the bottom (corresponding to 45°C) and top (corresponding to 37.5°C) boundary of the transport domain is presented in column 2 and column 3 of Table 16. Similarly, the brine composition in the reservoir (supposed to be leaking from the reservoir) resulting from the dissolution of CO_2 at a pressure of 105×10^5 Pa and 45°C for reactions considered in scenario 3 is presented in Table 17. At a pressure of 105×10^5 Pa, the concentration of dissolved CO_2 increased to a value of 1.08 mol/(kg water) from its background value of 1.98×10^{-4} mol/(kg water). Accordingly, the pH of the CO_2-saturated brine in the reservoir dropped to a value of 4.81 from its background value of 7.28. The boundary values of the resulting brine in terms of five component species involved in reactive transport are also presented in Table 17 (sub-index bc).

4.1.3. Paper IV

Background BGM provides the resident brine composition in the reservoir in equilibrium with the considered carbonate minerals calcite, dolomite and siderite. For the considered temperature gradient in the reservoir, columns 2 and 3 of Table 18 present the resident brine composition at the top (27°C) and bottom (34.5°C)

Table 18. The brine composition from BGM.

Species	Composition of the resident brine at the top boundary of the reservoir [mol/(kg water)]	Composition of the resident brine at the bottom boundary of the reservoir [mol/(kg water)]	Composition of the injected brine saturated with dissolved CO_2 [mol/(kg water)]
CO_{2aq}	2.89×10^{-4}	2.44×10^{-4}	0.90
HCO_3^-	4.58×10^{-3}	4.22×10^{-3}	4.74×10^{-3}
Na+	0.50	0.50	0.50
H^+	5.52×10^{-8}	5.08×10^{-8}	1.67×10^{-4}
OH^-	4.01×10^{-7}	5.15×10^{-7}	1.33×10^{-10}
CO_3^{2-}	1.61×10^{-5}	1.66×10^{-5}	5.53×10^{-9}
$NaHCO_{3aq}$	1.24×10^{-3}	1.10×10^{-4}	1.29×10^{-3}
Ca^{2+}	2.62×10^{-3}	2.40×10^{-3}	2.62×10^{-3}
Mg^{2+}	2.53×10^{-4}	2.25×10^{-4}	2.53×10^{-4}
Fe^{2+}	2.99×10^{-5}	2.68×10^{-5}	2.99×10^{-5}
$CaHCO_3^+$	5.31×10^{-5}	4.60×10^{-5}	5.48×10^{-5}
$MgHCO_3^+$	3.94×10^{-6}	3.28×10^{-6}	4.07×10^{-6}
$FeHCO_3^+$	6.87×10^{-7}	5.41×10^{-7}	7.09×10^{-7}

boundary of the reservoir, respectively. The pH of the resident brine was found as 7.26 and 7.29 at the top and bottom boundaries of the reservoir, respectively.

The composition of the injected brine (column 4 of Table 18) was obtained from CO_2 solubility modelling performed at a pressure of 41×10^5 Pa and temperature of 27°C, i.e., conditions representative of the upper boundary of the reservoir. The concentration of dissolved CO_2 was found to be 0.90 mol/(kg water) in the injected CO_2-saturated brine. The dissolved CO_2 resulted in a drop in pH from 7.26 to 3.78. Additionally, the conditions of the CO_2-saturated brine became highly undersaturated with respect to the minerals calcite, dolomite and siderite considered in the modelling. Solubility modelling shows that approximately 25.2 kg of brine fluid is needed to dissolve one kg of CO_2.

4.2. Reactive transport modelling

The fluid initially present in the transport domain (fractured caprock) was at chemical equilibrium with respect to the considered carbonate minerals (the conditions obtained from background BGM). The geochemical reactions were initiated by the leaking brine carrying a higher concentration of dissolved CO_2. The mixing of leaking CO_2-saturated brine with the resident fluid in the transport domain brought the solution in under-saturation conditions with respect to the considered carbonate minerals. The resulting undersaturated conditions initiated the dissolution of carbonate minerals, initially in the vicinity of the bottom inlet boundary.

4.2.1. Paper I

4.2.1.1. Base-case scenarios

The mixing of fluids (leaking CO_2-saturated brine with the resident fluid in the transport domain) caused the geochemical conditions to be below saturation with respect to calcite. Fig. 5a and b show the saturation state of the solution with respect to calcite right after the onset (1 s) of the simulation in scenarios 4 (without sorption) and 5 (with sorption), respectively. A larger spread of the under-saturating zone can be observed in the no-sorption scenario 4 compared to the sorption scenario 5. The sorption process retarded the species transport and thus lowered their spread in scenario 5.

The resulting calcite reaction rate [mol/(s-kg water)] at the onset (1 s) of the simulation in scenarios 4 (without sorption) and 5 (with sorption) is presented in Fig. 6a and b, respectively. In the rock matrix, the mineral calcite either dissolved or precipitated depending upon the spatial and temporal evolutions of geochemical conditions. In Fig. 6, the positive values of the reaction rate represent the calcite dissolution reaction rate and vice versa. The spread of the reaction zone (Fig. 6a and b) relates to the saturation state of calcite observed for the no-sorption scenario 4 and sorption scenario 5 in Fig. 5a and b. Although the spread of the reaction zone was lower in the sorption scenario 5 compared

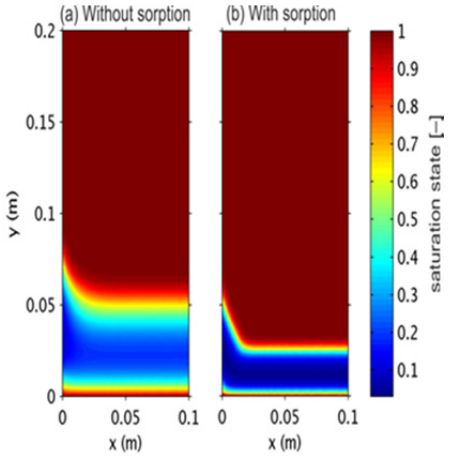

Fig. 5. Saturation state of calcite at the onset (1 s) of the simulation for (a) no-sorption scenario 4; and (b) sorption scenario 5 (Paper I).

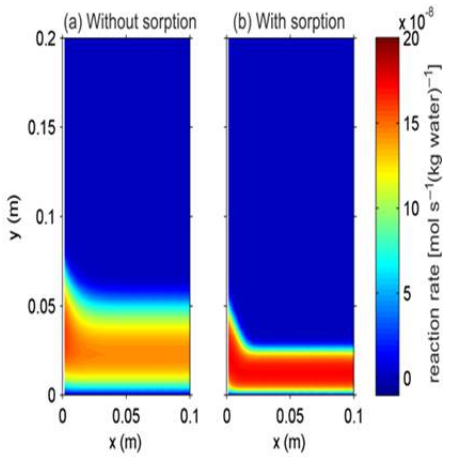

Fig. 6. Calcite reaction rate [mol/(s-kg water)] at the onset (1 s) of simulation; (a) no-sorption scenario 4; and (b) sorption scenario 5 (Paper I).

to that in scenario 4, the calcite dissolution reaction rate was higher in the former compared to the latter scenario (Fig. 6).

Calcite dissolution and precipitation caused variations in the medium porosity and thus the effective diffusivity in the rock matrix (Fig. 7). Figs. 7a and b show an enlarged view of variations in the medium porosity and effective diffusivity, respectively, near the bottom inlet boundary in the sorption scenario 5 after 500 years. Medium porosity and effective diffusivity reached nearly 0.18 and 5.21×10^{-10} [m^2/s], respectively, from their initial values of 0.12 and 3.66×10^{-10} [m^2/s]. The porosity variations have been mainly found near the bottom inlet boundary and up to 0.15 m along the conducting fracture.

According to the reaction stoichiometry, the dissolution reaction of the mineral calcite consumes H^+ ions from the solution while producing Ca^{2+} and HCO_3^- ions in the solution. The calcite dissolution reaction in the rock matrix that was driven by a higher concentration of CO_{2aq} and thus H^+ ions in the leaking brine resulted in the conversion/consumption of CO_{2aq} (Dreybrodt et al., 1996; Kaufmann and Dreybrodt, 2007). However, precipitation of calcite in the rock matrix may do the opposite and release CO_{2aq} back into the solution (Dreybrodt et al., 1997). Prevailing higher calcite dissolution compared to its precipitation in the rock matrix over the period of time resulted in the net conversion/consumption of dissolved CO_2 along the leakage pathway.

The quantities of CO_{2aq} entering the transport pathway (those leaked from the reservoir) and its conversion/consumption in geochemical reactions are presented in Fig. 8 for the no-sorption scenario 4 and sorption scenario 5 over the period of 500 years. Fig. 8a, b and c present, respectively, the cumulative quantities of CO_{2aq} entering the domain, its cumulative quantities consumed in

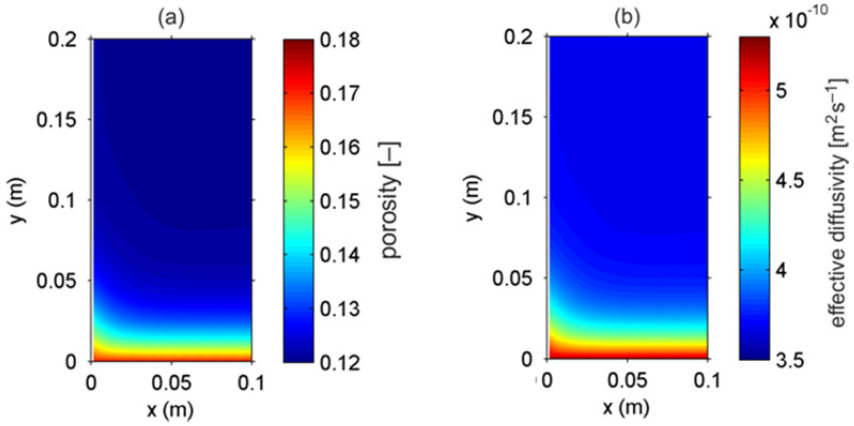

Fig. 7. Variations in medium porosity (a) and effective diffusivity (b) in the rock matrix due to calcite dissolution and precipitation in the sorption scenario 5 after 500 years (Paper I).

reactions and the cumulative consumption computed as a percentage.

It can be observed that the sorption process in scenario 5 caused higher mass inflows and mass consumption in geochemical reactions compared to that in the no-sorption scenario 4 (Fig. 8a, b). However, different trends were found for the percent mass consumption in these scenarios (Fig. 8c). The percent mass consumption in the no-sorption scenario 4 stays higher compared to scenario 5 during the initial times, and the opposite was observed towards the later times (Fig. 8c). The percentage mass consumption of CO_{2aq} in reactions was found to be 4.43% and 4.97% in scenario 4 and scenario 5, respectively, after 500 years (Table 19). The lower percent mass consumption in scenario 5 compared to scenario 4 in the initial times was (i) mainly because the percent mass consumption was computed in relation to mass inflows and (ii), to a lesser extent, a result of the decreased aqueous state mass available for reaction due to sorption.

In the initial period, sorption caused higher concentration gradients across the bottom inlet boundary due to the mass partitioning of CO_{2aq} between its aqueous and adsorbed states. The fixation of CO_{2aq} on rock surfaces decreases CO_{2aq} concentration in the aqueous state and causes higher concentration gradients and thus higher diffusive fluxes across the bottom inlet boundary during the initial period (row 4 of Table 19). However, the mass inflow decreased over the period of time due to the decrease in concentration gradients. Additionally, over the period of time, a lower saturation state with respect to calcite in the domain was found in the sorption scenario 5 compared to the no-sorption scenario 4. The sorption process lowered the species aqueous concentration, which resulted in a lower mineral saturation state for a fixed equilibrium constant. The lower saturation state of calcite thus caused higher overall calcite dissolution with higher CO_2 consumption in the sorption scenario 5 compared to the no-sorption scenario 4. Thus, over the period of time, decreased mass inflows but increased CO_2 consumption resulted in higher

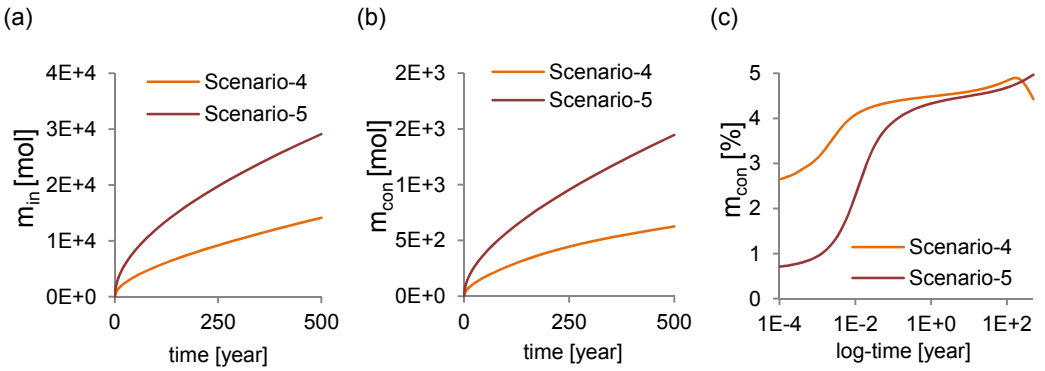

Fig. 8. Quantities of CO_{2aq} in the transport domain over 500 years; (a) cumulative mass entering the domain, (b) cumulative mass consumed, and (c) percentage mass consumed (Paper I).

percentage consumption of CO_2 towards the later times in the sorption scenario 5 compared to the no-sorption scenario 4.

The mass balance of CO_{2aq} in the transport domain (mass entering and leaving the domain, mass stored in aqueous and adsorbed states, mass consumed in reactions, etc.) for various reactive transport scenarios is presented in Table 19. The split of total mass entering the domain through the bottom inlet boundary is presented in terms of advective, dispersive and diffusive mass fluxes. Although mass transport in the fracture takes place by advection, dispersion and diffusion, whereas diffusion alone was the only transport process considered in the rock matrix, the total mass inflow through the bottom inlet boundary of the rock fracture was found to be lower than that entering through the inlet boundary of the rock matrix. This is because of the much smaller width (1 mm) of the rock fracture compared to the rock matrix (10 m) and the low velocity in the fracture. A very small error (less than 0.08%) in mass balance exists in all reactive transport scenarios (Table 19).

The retardation in the transport of dissolved CO_2 was analysed in the form of breakthrough curves (BTCs) representing its concentration at specific locations along the leakage pathway. The transport of CO_{2aq} along the fractured pathway was seen to be affected by various transport processes, including mass exchange between the fracture and rock matrix through matrix diffusion, sorption and geochemical reactions in the rock matrix. Fig. 9 presents the BTCs of leaking CO_{2aq} at various locations along the fracture for various base-case transport scenarios. Fig. 9a shows the BTC of CO_{2aq} at the top of the fracture (20 m from the bottom inlet boundary) for scenario 1. The least retardation was found in this transport scenario due to the absence of any mass exchange between the conducting fracture and the neighbouring rock matrix without sorption and geochemical reactions. In this scenario, the concentration quickly reached the boundary value.

Fig. 9b and c show the BTCs of CO_{2aq} at the midpoint of the fracture (10 m from the bottom inlet boundary) and the top of the fracture respectively for scenarios 2 through 5. The lower concentration in the reactive transport scenarios 4 and 5 compared to the corresponding mass transport scenarios 2 and 3 shows the

effect of geochemical reactions on the transport retardation. The highest retardation in transport can be observed in scenario 5, which represents the combined effects of the mass exchange between the fracture and the rock matrix through diffusion as well as sorption and geochemical reactions in the rock matrix. As a result of significant retardation caused by sorption, there was no visible increase in the concentration of CO_{2aq} at the top boundary in scenarios 3 and 5 (Fig. 9c).

4.2.1.2. Sensitivity analysis

Role of fluid velocity in fracture and sorption

Fig. 10 presents the trends of CO_2 consumption in geochemical reactions for various reactive transport scenarios 5.1 to 5.4 studied in the sensitivity analysis. These scenarios represent three different vertical velocities in the fracture and three different sorption partition coefficients. It can be observed that the cumulative consumption of CO_2 in reactions increases (Fig. 10a) whereas the percent consumption decreases (Fig. 10b) with an increase in the

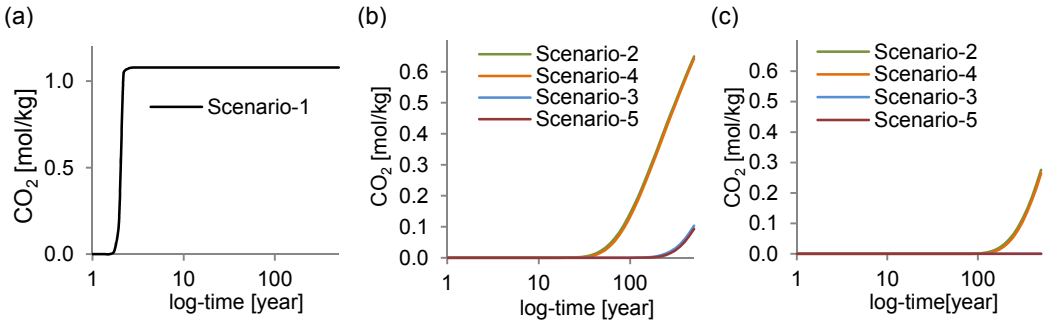

Fig. 9. Breakthrough curve of CO_{2aq} along the fracture at (a) the top boundary for scenario 1; (b) mid-way for scenarios 2 to 5 and; (c) the top boundary for scenarios 2 to 5 (Paper I).

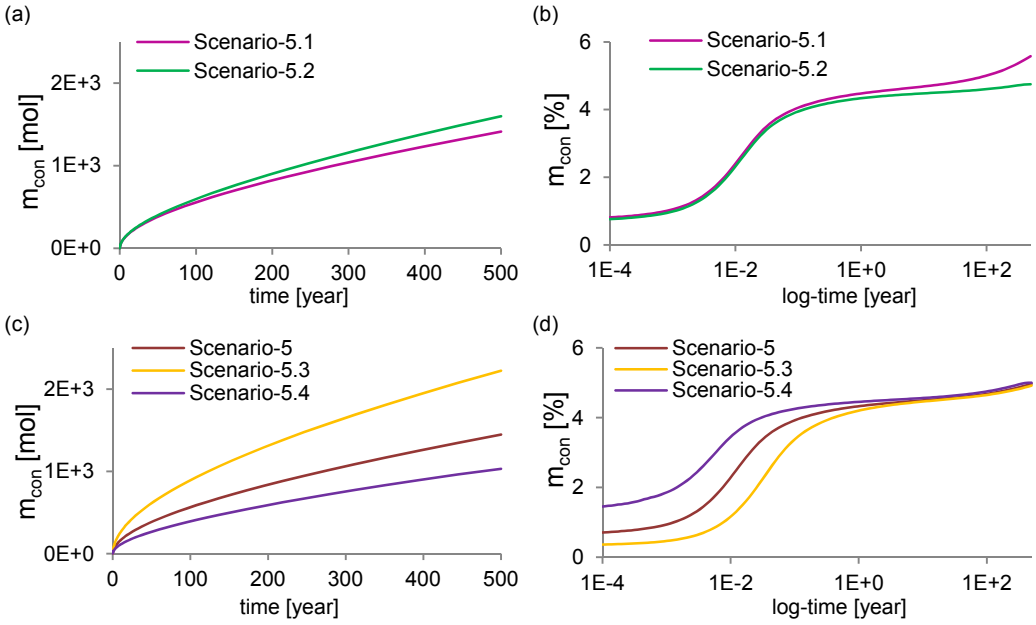

Fig. 10. Consumption of CO_{2aq} in the transport domain over 500 years; (a) cumulative consumption in scenarios 5.1 and 5.2, (b) percent consumption in scenarios 5.1 and 5.2, (c) cumulative consumption in scenarios 5, 5.3 and 5.4, and (d) percent consumption in scenarios 5, 5.3 and 5.4 (Paper I).

vertical velocity in the fracture for the same sorption in scenarios 5.1 and 5.2. In addition, the cumulative consumption of CO_2 in reactions increases (Fig. 10c) whereas percent consumption decreases (Fig. 10d) with an increase in the sorption partition coefficient for the same velocity in the fracture in scenarios 5, 5.3 and 5.4. The observed decrease in the percentage of CO_2 consumption was due to the increase of mass inflows with an increase in velocity and the partition coefficient. The base-case scenario 5, representing the medium values of velocity in the fracture and partition coefficient, exhibits medium levels of CO_2 percentage consumption. Sorption also caused partitioning of the total mass into aqueous and adsorbed states as a function of the considered partitioning coefficient (Table 19).

Role of the temperature and diffusion coefficient

The effects of temperature on the mass of CO_{2aq} entering the domain and its consumption in geochemical reactions can be seen in Fig. 11, which compares the results between scenarios 5, 5a and 5b. For the same diffusion coefficient in scenarios 5a and 5, there was a lower mass inflow in scenario 5a compared to scenario 5 due to the lower concentration of CO_{2aq} in the leaking brine in the former [1.06 mol/(kg water)] than that in the latter scenario [1.08 mol/(kg water)]. The higher temperature considered in scenarios 5a and 5b (60°C) resulted in a lower concentration of CO_{2aq} in the leaking brine compared to that in scenario 5 (45°C). Alternately, for the same temperature and thus the same CO_{2aq} concentration in the leaking brine, the higher mass inflow in scenario 5b compared to that in scenario 5a was due to the higher diffusion coefficient considered in the former [4.05×10^{-9} m^2/s] than that used in the latter scenario [3.05×10^{-9} m^2/s].

We observe the varying trends in the percentage consumption of CO_2 between the high-temperature scenarios 5a and 5b and the low-temperature scenario 5. In the initial period, the observed higher percentage of CO_2 consumption in the high-temperature scenarios 5a and 5b compared to the low-temperature scenario 5 is due to the higher calcite reaction rate constant [9.44×10^{-9} mol/(s-m^2)] in the former scenarios than that in the latter [4.63×10^{-9} mol/(s-m^2)].

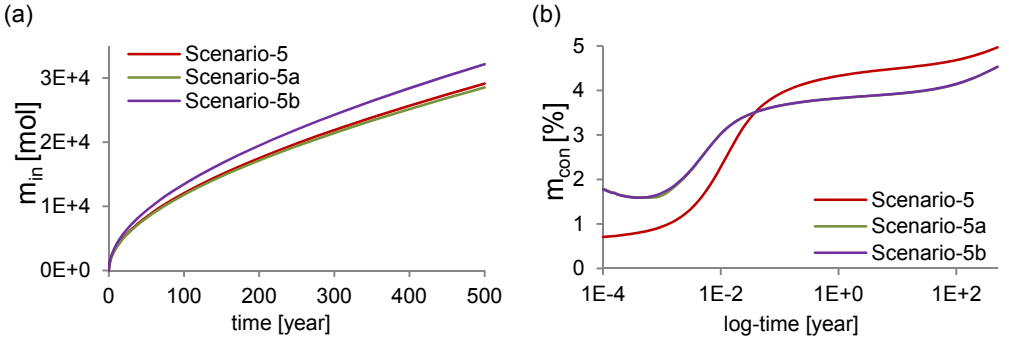

Fig. 11. The effects of the temperature and diffusion coefficient on (a) the mass of CO_{2aq} inflows and (b) the percent consumption of CO_2 in the reactions (Paper I).

Table 19. Mass [mol] balance of CO_{2aq} in the transport domain for various reactive transport scenarios after 500 years.

Scenarios	Scenario 4	Scenario 5	Scenario 5.1	Scenario 5.2	Scenario 5.3	Scenario 5.4	Scenario 5a	Scenario 5b
Total mass entering the domain	1.41×10^{4}	2.91×10^{4}	2.59×10^{4}	3.37×10^{4}	4.53×10^{4}	2.06×10^{4}	2.85×10^{4}	3.21×10^{4}
Mass entering the domain due to advection	5.39×10^{3}	5.39×10^{3}	5.39×10^{2}	1.08×10^{4}	5.39×10^{3}	5.39×10^{3}	5.29×10^{3}	5.29×10^{3}
Mass entering the domain due to diffusion	8.73×10^{3}	2.37×10^{4}	2.53×10^{4}	2.29×10^{4}	3.99×10^{4}	1.53×10^{4}	2.32×10^{4}	2.68×10^{4}
Mass entering the domain due to dispersion	9.15×10^{-5}	2.96×10^{-4}	2.96×10^{-5}	2.52×10^{-4}	5.87×10^{-4}	1.71×10^{-4}	2.85×10^{-4}	3.04×10^{-4}
Mass leaving the domain	4.27×10^{2}	9.63×10^{-1}	9.11×10^{-2}	2.75×10^{1}	9.11×10^{-1}	1.85×10^{1}	7.44×10^{-1}	8.12×10^{-1}
Mass stored in an aqueous state	1.31×10^{4}	4.68×10^{3}	4.13×10^{3}	5.42×10^{3}	2.77×10^{3}	7.41×10^{3}	4.60×10^{3}	5.18×10^{3}
Mass stored in an adsorbed state	0.00	2.30×10^{4}	2.03×10^{4}	2.66×10^{4}	4.03×10^{4}	1.22×10^{4}	2.26×10^{4}	2.55×10^{4}
Mass converted in geochemical reactions	6.25×10^{2}	1.45×10^{3}	1.41×10^{3}	1.60×10^{3}	2.22×10^{3}	1.03×10^{3}	1.29×10^{3}	1.46×10^{3}
CO_2 conversion over 500 years (%)	4.43	4.97	5.46	4.75	4.91	4.99	4.53	4.53
Error in mass balance (%)	5.99×10^{-2}	7.33×10^{-2}	8.27×10^{-2}	6.19×10^{-2}	7.63×10^{-2}	6.77×10^{-2}	7.37×10^{-2}	7.54×10^{-2}

The increase in temperature in scenarios 5a and 5b resulted in a higher calcite reaction rate constant. However, the increase in temperature in scenarios 5a and 5b lowered the calcite equilibrium constant (K_{cal} = 16.34) compared to that in the low-temperature scenario 5 (K_{cal} = 26.76). With a decreasing equilibrium constant, the saturation state with respect to calcite was reached at decreasing concentrations of the reaction products (Ca^{2+} and HCO_3^-) and increasing concentrations of reactants (H^+). This phenomenon resulted in a lower consumption of H^+ ions in the calcite reaction, which in turn lowered the consumption of dissolved CO_2 towards the later period in the high-temperature scenarios 5a and 5b. Over the period of 500 years, the consumption of CO_2 in the reactions was found to be 4.53% in the high-temperature scenarios 5a and 5b and 4.97% in the low-temperature scenario 5 (Table 19).

4.2.2. Paper II

Porosity and permeability variations were found in the conducting fracture as well as in the rock matrix due to the calcite dissolution and precipitation considered in both these domains. Fig. 12a and b present the variations in medium porosity and permeability, respectively, in the rock matrix for the base-case scenario 2 after 500 years. At the bottom inlet boundary, the porosity of the rock matrix increased by nearly 42% and reached 0.17 from its initial value of 0.12, whereas the permeability reached a value of 1.337×10^{-12} m^2 from its initial value of 3.71×10^{-13} m^2. These increases were observed at and near the bottom inflow boundary due to the continuous calcite dissolution taking place there. However, a negligible decrease in porosity and permeability was also found towards the top of the domain (closer to the fracture) as a result of the small calcite precipitation.

Table 20 presents the mass balance of dissolved CO_2 in the transport domains after 500 years for various scenarios. Table 20 divides the total mass entering the domain into mass entered due to advection, dispersion and diffusion through the bottom inlet

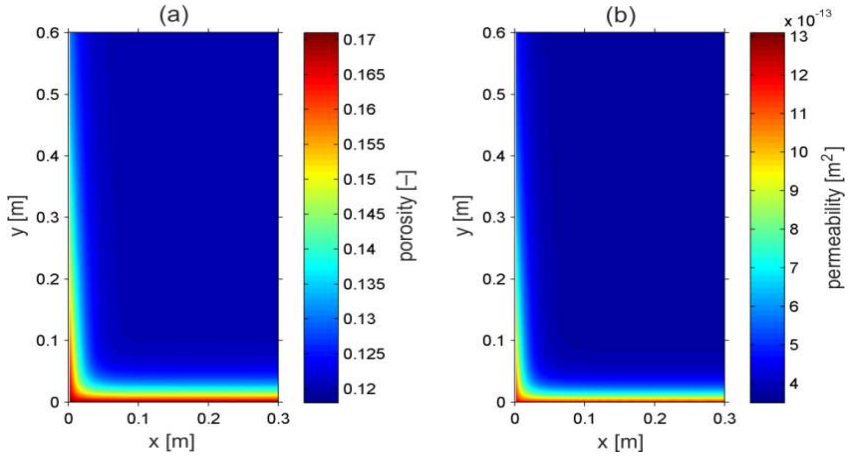

Fig. 12. Porosity [-] (a) and permeability [m^2] (b) of the rock matrix in the reactive transport scenario 2 after 500 years (Paper II).

boundary of both the fracture and the rock matrix. It can be seen that the advective transport scenarios 2 and 4 resulted in higher mass inflows of CO_{2aq} (Table 20) and higher cumulative consumption in reactions compared to the corresponding diffusive transport scenarios 1 and 3 (Fig. 13a and c). Additionally, in the advective transport scenarios 2 and 4, higher calcite dissolution took place in the transport domain compared to the corresponding diffusive transport scenarios 1 and 3 (row 6 of Table 21). Although the cumulative consumption of CO_{2aq} in reactions is higher in the advective transport scenarios 2 and 4 compared to the diffusive transport scenarios 1 and 3, the opposite is found for the percentage of CO_2 consumption (Fig. 13a vs. 13b and Fig. 13c vs. 13d). This is because advective transport dominates the mass inflows through the bottom boundary, hence promoting a lower percent consumption despite having a higher cumulative consumption in advective transport scenarios compared to diffusive transport scenarios. It can also be observed that the sorption process caused higher mass inflows of CO_{2aq} and its consumption in reactions in scenarios 3 and 4 compared to the corresponding no-sorption scenarios 1 and 2 (Table 20).

Role of fluid velocity and dispersivity

The higher velocity in scenario 6 caused higher cumulative mass inflows (Table 20) of CO_{2aq} and higher consumption in reactions compared to scenarios 2 and 5 (Fig. 13e). In addition, the mass of calcite dissolved with the associated production of Ca^{2+}, and the pore volumes all increased with increasing fluid velocity in scenario 6 compared to scenarios 2 and 5 (Table 21). Although the cumulative consumption of CO_{2aq} in reactions increased with fluid velocity, its percentage consumption decreased with fluid velocity (Fig. 13e vs. 13f). This is also due to calculating the percentage consumption of CO_{2aq} in relation to the mass inflows, as was observed for scenarios 1, 2, 3 and 4. Alternately, for the same fluid velocity, higher dispersivity in scenario 8 caused higher CO_{2aq} mass inflows (Table 20) and consumption in reactions compared to the corresponding scenarios 2 and 7 (Fig. 13g). Additionally, the mass of calcite dissolved with the associated production of Ca^{2+} and the pore volume all increased for an increase in dispersivity in scenario 8 compared to scenarios 2 and 7 (Table 21). However, an increase in dispersivity caused increased cumulative consumption of CO_{2aq}, as well as its percentage consumption (Fig. 13g and 13h).

Moreover, in all the reactive transport scenarios, higher calcite dissolution took place in the fracture than in the rock matrix, relative to the initial mass of calcite present, due to the higher advective velocity in the fracture than in the rock matrix (rows 3 and 5 of Table 21). Additionally, in all the reactive transport scenarios, the mass of calcite consumed was found to be equal to the mass of Ca^{2+} produced (rows 6 and 7 of Table 21) except for a mass balance error of less than 0.1%. Furthermore, in all the reactive transport scenarios, the CO_{2aq} consumption in reactions was found to be directly related to the calcite dissolution with the associated production of Ca^{2+} and increase in pore volume.

Table 20. Mass [mol] balance of CO_{2aq} in the transport domain for various reactive transport scenarios after 500 years.

Reactive transport scenarios	Scenario 1	Scenario 2	Scenario 3	Scenario 4	Scenario 5	Scenario 6	Scenario 7	Scenario 8
Total mass entering the domain	5.98×10^{4}	5.26×10^{5}	1.39×10^{5}	5.62×10^{5}	2.69×10^{5}	7.85×10^{5}	5.29×10^{5}	5.33×10^{5}
Mass entering due to advection (fracture)	5.70×10^{3}	5.56×10^{3}	6.04×10^{3}	5.78×10^{3}	2.77×10^{3}	8.31×10^{3}	5.60×10^{3}	5.61×10^{3}
Mass entering due to diffusion (fracture)	1.79	2.94×10^{-1}	3.85	1.68	6.23×10^{-1}	1.89×10^{-1}	3.14×10^{-1}	3.24×10^{-1}
Mass entering due to dispersion (fracture)	3.19×10^{3}	5.12×10^{2}	7.21×10^{3}	3.02×10^{3}	5.42×10^{2}	4.95×10^{2}	1.10×10^{3}	1.70×10^{3}
Mass entering due to advection (matrix)	0.00	5.12×10^{5}	0.00	5.12×10^{5}	2.55×10^{5}	7.68×10^{5}	5.12×10^{5}	5.12×10^{5}
Mass entering due to diffusion (matrix)	5.09×10^{4}	4.86×10^{3}	1.26×10^{5}	2.49×10^{4}	9.03×10^{3}	3.38×10^{3}	4.75×10^{3}	4.68×10^{3}
Mass entering due to dispersion (matrix)	0.00	3.12×10^{3}	0.00	1.60×10^{4}	1.45×10^{3}	4.85×10^{3}	6.11×10^{3}	9.04×10^{3}
Mass leaving the domain (fracture)	9.24×10^{-1}	1.69×10^{2}	9.14×10^{-1}	9.14×10^{-1}	4.74×10^{-1}	2.03×10^{3}	2.92×10^{2}	4.03×10^{2}
Mass leaving the domain (matrix)	0.00	3.32×10^{3}	0.00	8.65×10^{1}	4.32×10^{1}	1.35×10^{5}	6.26×10^{3}	9.40×10^{3}
Mass stored in an aqueous state	5.59×10^{4}	5.19×10^{5}	2.22×10^{4}	9.31×10^{4}	2.66×10^{5}	6.42×10^{5}	5.18×10^{5}	5.18×10^{5}
Mass stored in an adsorbed state	0.00	0.00	1.09×10^{5}	4.60×10^{5}	0.00	0.00	0.00	0.00
Mass converted in geochemical reactions	3.86×10^{3}	4.09×10^{3}	7.57×10^{3}	8.49×10^{3}	3.50×10^{3}	4.42×10^{3}	4.81×10^{3}	5.43×10^{3}
Mass consumption of CO_2 after 500 years (%)	6.46	7.79×10^{-1}	5.45	1.51	1.30	5.63×10^{-1}	9.10×10^{-1}	1.02
Error in mass balance (%)	1.82×10^{-2}	-9.16×10^{-2}	1.97×10^{-2}	1.34×10^{-2}	5.47×10^{-3}	4.83×10^{-2}	-1.01×10^{-1}	-1.03×10^{-1}

Table 21. Mass [mol] balance of calcite and Ca^{2+} and increase in the pore volume [m^3] in the transport domain for various reactive transport scenarios after 500 years.

Reactive transport scenarios	Scenario 1	Scenario 2	Scenario 3	Scenario 4	Scenario 5	Scenario 6	Scenario 7	Scenario 8
Mass of calcite dissolved in the fracture	7.26×10^{0}	7.33×10^{0}	1.24×10^{1}	1.36×10^{1}	4.65×10^{0}	4.88×10^{0}	7.43×10^{0}	8.54×10^{0}
Decrease in mass in the fracture (%)	2.31×10^{0}	2.33×10^{0}	3.94×10^{0}	4.33×10^{0}	1.48×10^{0}	1.55×10^{0}	2.36×10^{0}	2.72×10^{0}
Mass of calcite dissolved in the rock matrix	3.81×10^{3}	4.07×10^{3}	7.58×10^{3}	8.36×10^{3}	3.48×10^{3}	4.43×10^{3}	4.80×10^{3}	5.40×10^{3}
Decrease in mass in the rock matrix (%)	1.10×10^{-2}	1.18×10^{-2}	2.19×10^{-2}	2.42×10^{-2}	1.01×10^{-2}	1.28×10^{-2}	1.39×10^{-2}	1.56×10^{-2}
Total mass of calcite dissolved	3.81×10^{3}	4.08×10^{3}	7.59×10^{3}	8.38×10^{3}	3.49×10^{3}	4.43×10^{3}	4.80×10^{3}	5.41×10^{3}
Mass of Ca^{2+} produced	3.81×10^{3}	4.08×10^{3}	7.58×10^{3}	8.37×10^{3}	3.49×10^{3}	4.43×10^{3}	4.81×10^{3}	5.41×10^{3}
Increase in pore volume in the fracture	2.68×10^{-4}	2.71×10^{-4}	4.57×10^{-4}	5.02×10^{-4}	1.72×10^{-4}	1.80×10^{-4}	2.74×10^{-4}	3.15×10^{-4}
Increase in pore volume in the rock matrix	1.41×10^{-1}	1.50×10^{-1}	2.80×10^{-1}	3.09×10^{-1}	1.29×10^{-1}	1.63×10^{-1}	1.77×10^{-1}	1.99×10^{-1}
Total increase in pore volume	1.41×10^{-1}	1.51×10^{-1}	2.80×10^{-1}	3.09×10^{-1}	1.29×10^{-1}	1.64×10^{-1}	1.77×10^{-1}	2.00×10^{-1}
Error in mass balance (%)	-1.03×10^{-1}	-4.75×10^{-2}	1.42×10^{-1}	4.40×10^{-2}	6.16×10^{-3}	5.32×10^{-2}	-1.07×10^{-1}	-1.13×10^{-1}

Significance of the consideration of advection and dispersion in addition to diffusion in the rock matrix

Including advection and dispersion in addition to diffusion as a transport mechanism in the rock matrix caused a 6.04% higher consumption of CO_2 in the reactions in scenario 2 compared to the corresponding diffusive transport scenario 1 and a 12.20% higher consumption in scenario 4 compared to the corresponding diffusive transport scenario 3.

Increasing the fluid velocity resulted in higher CO_{2aq} consumption in reactions. Scenario 2 (representing a fluid velocity of 10 m/year in the fracture) and scenario 6 (representing a fluid velocity of 15 m/year in the fracture) caused 16.8% and 26.10%, respectively, higher CO_{2aq} consumption compared to scenario 5 (representing a fluid velocity of 5 m/year in the fracture).

In addition, an increase in dispersivity caused higher CO_{2aq} consumption in reactions. Scenario 7 (representing a longitudinal dispersivity of 20 m) and scenario 8 (representing a longitudinal dispersivity of 30 m) caused higher consumption by 17.60% and 32.60%, respectively, compared to scenario 2 (representing a longitudinal dispersivity of 10 m).

These observed differences in CO_{2aq} mass consumption in reactions show the significance of (i) including advection and dispersion in addition to diffusion in the rock matrix, (ii) variations in the fluid vertical velocity and (iii) the magnitude of the longitudinal dispersivity along the leakage pathway.

4.2.3. Paper III

An initial vertical fluid velocity of nearly 20 and 0.04 m/year in the conducting fracture and the rock matrix, respectively, resulted from an applied excess pressure of 500 Pa at the bottom inlet boundary. These velocities are representative for sedimentary basins (Bachu et al., 1994). Variations in porosity and permeability were found due to the dissolution/precipitation of carbonate minerals (calcite and dolomite) in both the conducting fracture and the rock matrix. However, the porosity increase in the rock matrix was observed close to and along the fracture. The porosity increased up to 0.603 and 0.126 after 500 years from the initial values of 0.60 and 0.12 in the fracture and rock matrix, respectively. Variations in permeability linked to porosity also affected the fluid velocity in the fracture.

Fig. 14 presents the cumulative quantities of CO_{2aq} leaking from the reservoir, its consumption in reactions and its percentage consumption for various transport scenarios over 500 years. For the same advection, dispersion and diffusion, the amount of CO_{2aq} that entered the domain remained nearly the same in all the scenarios. However, its conversion in reactions was a function of the considered geochemical reactions. The simplified geochemical system considered in scenario 1 resulted in the lowest consumption of CO_2 in reactions compared to the corresponding scenarios 2 and 3 (Fig. 14c). Inclusion of one additional reaction (R5) in scenario 2 resulted in CO_{2aq} conversion nearly 7.85% higher than that in scenario 1. Similarly inclusion of three

additional reactions ((R5), (R6) and (R8)) in scenario 3 resulted in CO_{2aq} conversion nearly 11.26% higher than that in scenario 1. The species Ca^{2+} and Mg^{2+} are produced in the dissolution of the minerals calcite and dolomite and, in dissolved form, reacted with HCO_3^- to form the species $CaHCO_3^+$ and $MgHCO_3^+$. The formation of metal bicarbonate ions reduces the concentration of metal (Ca^{2+} and Mg^{2+}) ions in the solution. This decrease in the concentrations of Ca^{2+}, Mg^{2+} and HCO_3^- from the solution enhances the dissolution process of the considered minerals, which in turn increases the CO_2 consumption. Thus, including the species $CaHCO_3^+$ and $MgHCO_3^+$ in the analysis through the involved equilibrium and kinetic reactions of calcite and dolomite enhanced the CO_2 consumption in scenarios 3 and 4 compared to the consumption in scenarios 1 and 2.

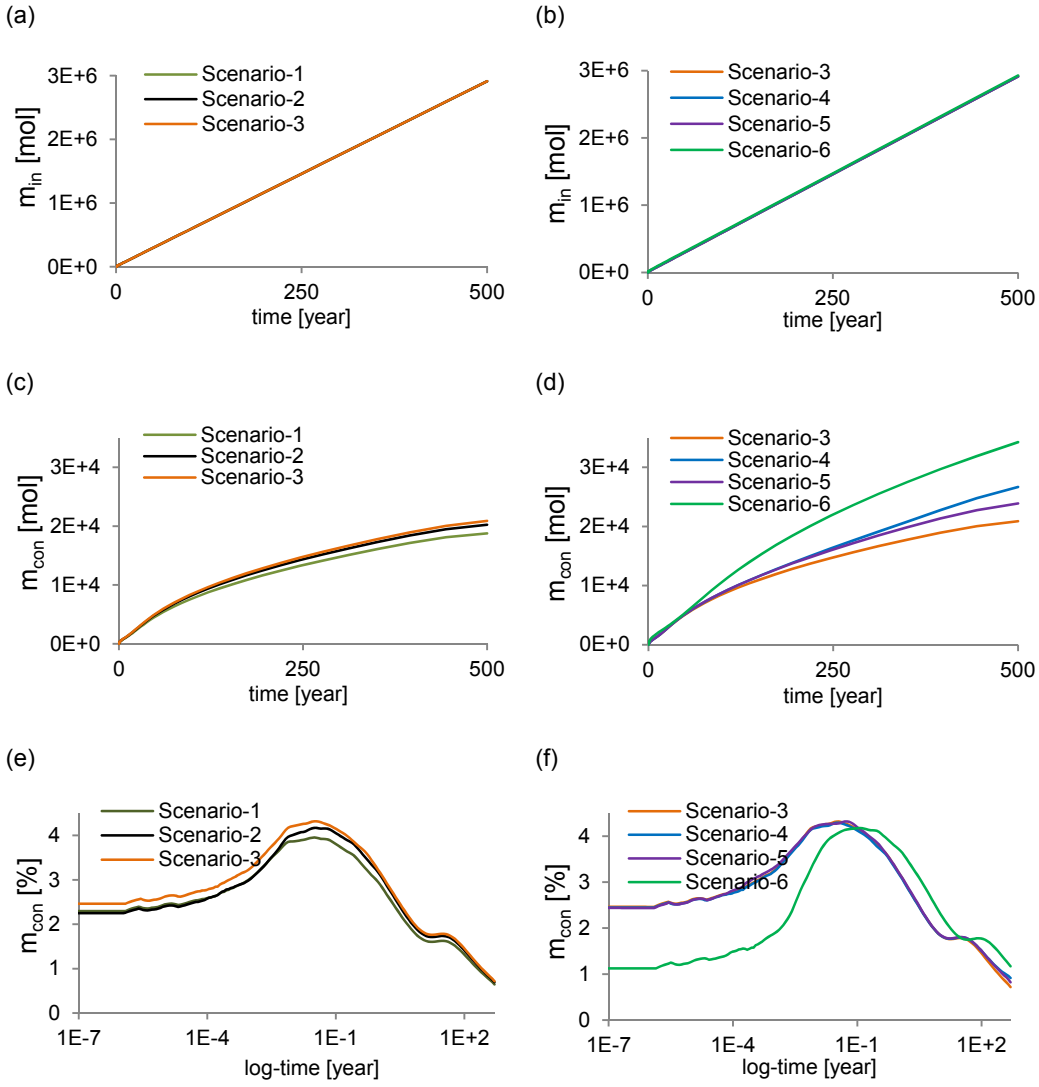

Fig. 14. Mass of CO_{2aq} in the transport domain over 500 years; (a) mass inflows in scenarios 1 to 3, (b) mass inflows in scenarios 3 to 6, (c) cumulative consumption in reactions in scenarios 1 to 3, (d) cumulative consumption in reactions in scenarios 3 to 6, (e) percent consumption in reactions in scenarios 1 to 3, and (f) percent consumption in reactions in scenarios 3 to 6 (Paper III).

For scenarios 3 to 6 (representing the extended geochemical system), the lowest conversion was found in scenario 3, whereas it was highest in scenario 6 (Fig. 14d). The vertical temperature gradient along the transport pathway considered in scenario 4 caused the CO_{2aq} consumption in the reactions to be nearly 27.84% higher than in scenario 3, which assumed a constant temperature along the transport domain. Inclusion of heat transport by leaking CO_2-saturated brine along the transport pathway in scenario 5, caused an approximately 14.45% higher CO_{2aq} consumption in reactions compared to the constant-temperature scenario 3. The sorption process in scenario 6 caused the CO_{2aq} consumption to be 43.39% higher than that in the corresponding no-sorption scenario 5.

The lower temperature towards the top of the domain in scenario 4 increases the equilibrium constant of the minerals calcite and dolomite. Due to the higher equilibrium constant, the saturation state of these minerals is reached at relatively higher concentrations of the reaction products Ca^{2+}, Mg^{2+} and HCO_3^- and a lower concentration of the reactant H^+. This phenomenon resulted in higher consumption of H^+ ions in these mineral reactions, which in turn caused higher consumption of dissolved CO_2. Having included heat transport by leaking brine in the analysis in scenario 5 increased the otherwise prevailing temperature in scenario 4 along the transport pathway. The resulting increase in temperature along the transport domain caused a decrease in the equilibrium constant of calcite and dolomite, which lowers the CO_2 consumption in scenario 5 compared to scenario 4. In all the reactive transport scenarios, the trends of percentage consumption (Fig. 14e and f) are similar to those of cumulative consumption of CO_{2aq} (Fig. 14c and d) with the exception of the sorption scenario 6 (Section 4.2.1.1 is referred for a related explanation).

The mass balance of leaking CO_{2aq} in the transport domain for various studied reactive transport scenarios after 500 years is presented in Table 22. The higher mass inflows in scenario 6 compared to the rest of the scenarios, through the bottom inlet boundary, was mainly due to higher dispersion induced by sorption. The consumption of CO_{2aq} in reactions was found to be 0.64, 0.69, 0.72, 0.92, 0.82 and 1.17% in the reactive transport scenarios 1 to 6, respectively. Compared to the conversion of CO_{2aq} in reactions in scenario 1, almost 7.85, 11.26, 42.23, 27.34, and 82.59% higher conversion was found in scenarios 2 to 6, respectively. Table 23 provides the mass balance of included carbonate minerals (calcite and dolomite) and associated component species u_{Ca} (defined as the sum of Ca^{+2} and $CaHCO_3^{+1}$) and u_{Mg} (sum of Mg^{+2} and $MgHCO_3^{+1}$). The higher velocity in the fracture caused higher mineral dissolution in the fracture compared to the rock matrix (row 5 vs. 6 and row 10 vs. 11 in Table 23).

.

Table 22. Mass [mol] balance of CO_{2aq} for the studied reactive transport scenarios after 500 years.

Reactive transport scenarios	Scenario 1	Scenario 2	Scenario 3	Scenario 4	Scenario 5	Scenario 6
Total mass entering the domain	2.91×10^{6}	2.91×10^{6}	2.91×10^{6}	2.91×10^{6}	2.91×10^{6}	2.93×10^{6}
Mass entering due to advection (fracture)	1.02×10^{4}	1.03×10^{4}	1.03×10^{4}	1.03×10^{4}	1.03×10^{4}	1.04×10^{4}
Mass entering due to diffusion (fracture)	1.18×10^{-1}	1.18×10^{-1}	1.18×10^{-1}	1.19×10^{-1}	1.19×10^{-1}	3.16×10^{-1}
Mass entering due to dispersion (fracture)	7.72×10^{1}	7.74×10^{1}	7.74×10^{1}	7.77×10^{1}	7.76×10^{1}	2.08×10^{2}
Mass entering due to advection (matrix)	2.90×10^{6}	2.90×10^{6}	2.90×10^{6}	2.90×10^{6}	2.90×10^{6}	2.90×10^{6}
Mass entering due to diffusion (matrix)	4.33×10^{3}	4.33×10^{3}	4.34×10^{3}	4.35×10^{3}	4.35×10^{3}	1.17×10^{4}
Mass entering due to dispersion (matrix)	2.94×10^{3}	2.95×10^{3}	2.95×10^{3}	2.96×10^{3}	2.95×10^{3}	7.92×10^{3}
Mass leaving the domain (fracture)	2.03×10^{2}	2.02×10^{2}	2.01×10^{2}	2.00×10^{2}	1.99×10^{2}	2.04
Mass leaving the domain (matrix)	1.10×10^{4}	1.09×10^{4}	1.08×10^{4}	1.05×10^{4}	1.07×10^{4}	5.87×10^{2}
Mass stored in an aqueous state	2.88×10^{6}	2.88×10^{6}	2.88×10^{6}	2.88×10^{6}	2.88×10^{6}	1.09×10^{6}
Mass stored in an adsorbed state	0.00	0.00	0.00	0.00	0.00	1.80×10^{6}
Mass converted in geochemical reactions	1.88×10^{4}	2.02×10^{4}	2.09×10^{4}	2.67×10^{4}	2.39×10^{4}	3.43×10^{4}
Mass conversion of CO_{2aq} after 500 years (%)	6.44×10^{-1}	6.95×10^{-1}	7.17×10^{-1}	9.16×10^{-1}	8.20×10^{-1}	1.17
Error in mass balance (%)	-4.81×10^{-2}	-4.81×10^{-2}	-5.02×10^{-2}	-5.02×10^{-2}	-4.81×10^{-2}	2.61×10^{-3}

Table 23. Mass [mol] balance of minerals (calcite and dolomite), associated component species (u_{Ca} and u_{Mg}) and pore volume [m^3] for various reactive transport scenarios after 500 years.

Reactive transport scenario	Scenario 1	Scenario 2	Scenario 3	Scenario 4	Scenario 5	Scenario 6
Mass of calcite dissolved in the fracture	1.53×10^{1}	1.54×10^{1}	1.43×10^{1}	1.42×10^{1}	1.41×10^{1}	2.17×10^{1}
Mass of calcite dissolved in the rock matrix	1.92×10^{4}	2.06×10^{4}	1.81×10^{4}	2.25×10^{4}	2.03×10^{4}	3.00×10^{4}
Total mass of calcite dissolved	1.92×10^{4}	2.06×10^{4}	1.81×10^{4}	2.25×10^{4}	2.04×10^{4}	3.00×10^{4}
Decrease in mass of calcite in the fracture (%)	1.95	1.96	1.82	1.80	1.79	2.76
Decrease in mass of calcite in the rock matrix (%)	8.87×10^{-3}	9.52×10^{-3}	8.39×10^{-3}	1.04×10^{-2}	9.42×10^{-3}	1.39×10^{-2}
Mass of dolomite dissolved in the fracture	0.00	0.00	1.37	1.41	1.39	2.11
Mass of dolomite dissolved in the rock matrix	0.00	0.00	1.47×10^{3}	2.29×10^{3}	1.87×10^{3}	2.53×10^{3}
Total mass of dolomite dissolved	0.00	0.00	1.47×10^{3}	2.29×10^{3}	1.88×10^{3}	2.53×10^{3}
Decrease in mass of dolomite in the fracture (%)	0.00	0.00	2.06	2.12	2.08	3.16
Decrease in mass of dolomite in the rock matrix (%)	0.00	0.00	7.99×10^{-3}	1.24×10^{-2}	1.02×10^{-2}	1.38×10^{-2}
Dolomite dissolved compared to calcite (%)	0.00	0.00	8.10	1.02×10^{1}	9.21	8.44
Mass of u_{Ca} produced	1.93×10^{4}	2.07×10^{4}	1.97×10^{4}	2.49×10^{4}	2.23×10^{4}	3.26×10^{4}
Mass of u_{Mg} produced	0.00	0.00	1.48×10^{3}	2.30×10^{3}	1.88×10^{3}	2.54×10^{3}
Mass of u_{Ca} and u_{Mg} produced	1.93×10^{4}	2.07×10^{4}	2.12×10^{4}	2.72×10^{4}	2.42×10^{4}	3.51×10^{4}
Net mass of u_{Ca} produced	1.93×10^{4}	2.07×10^{4}	1.82×10^{4}	2.26×10^{4}	2.04×10^{4}	3.01×10^{4}
Error in overall mass balance (%)	-3.87×10^{-1}	-4.03×10^{-1}	-3.57×10^{-1}	-4.09×10^{-1}	-3.43×10^{-1}	-8.86×10^{-2}
Increase in pore volume in the fracture	5.66×10^{-4}	5.69×10^{-4}	6.09×10^{-4}	6.07×10^{-4}	6.03×10^{-4}	9.26×10^{-4}
Increase in pore volume in the rock matrix	7.08×10^{-1}	7.60×10^{-1}	7.57×10^{-1}	9.66×10^{-1}	8.63×10^{-1}	1.26
Total increase in pore volume	7.08×10^{-1}	7.60×10^{-1}	7.58×10^{-1}	9.66×10^{-1}	8.64×10^{-1}	1.26
Increase in pore volume in the fracture (%)	3.77×10^{-1}	3.79×10^{-1}	4.06×10^{-1}	4.05×10^{-1}	4.02×10^{-1}	6.17×10^{-1}
Increase in pore volume in the rock matrix (%)	1.89×10^{-2}	2.03×10^{-2}	2.02×10^{-2}	2.58×10^{-2}	2.30×10^{-2}	3.36×10^{-2}

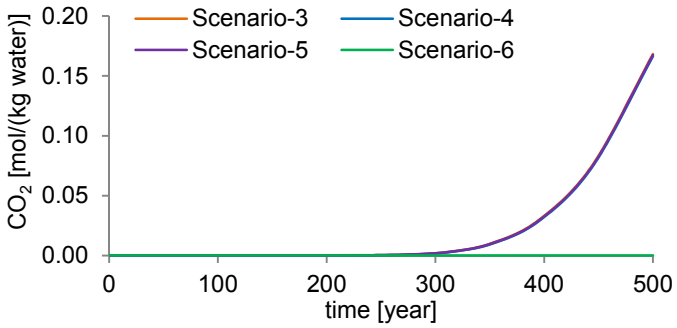

Fig. 15. BTCs of CO_{2aq} at a distance of 250 m along the fracture from the bottom inlet boundary for reactive transport scenarios 3 through 6 over a period of 500 years (Paper III).

Additionally, compared to calcite, the dissolution of dolomite remained lower than 10.2% in all the studied reactive transport scenarios, which resulted in lower production of u_{Mg} than u_{Ca} (row 13 vs. 14 of Table 23 for scenarios 3 to 7). Furthermore, the mass of minerals and associated species u_{Ca} and u_{Mg} was conserved except for an error of less than 0.41% in all the reactive transport scenarios.

Retardation in the transport of migrating CO_{2aq} was analysed by comparing BTCs derived along the fractured pathway. Fig. 15 presents the BTCs of CO_{2aq} at a distance of 250 m from the bottom inlet boundary for reactive transport scenarios 3 to 6. The concentration of CO_{2aq} was found to be approximately 0.17 mol/(kg water) as compared to the inlet boundary value of 1.08 mol/(kg water) in the reactive transport scenarios 3 through 5 after 500 years. Due to significant transport retardation in scenario 6, mainly caused by sorption, no observable increase in concentration of leaking CO_{2aq} was noticed at 250 m for a fluid velocity of nearly 20 m/year and partition coefficient of 2.5×10^{-4} m^3/kg.

4.2.4. Paper IV

In the studied injection scenarios, a total of nearly 2×10^5 tonnes of CO_{2aq} was injected in the reservoir in 10 years (Fig. 17 and Table 24). For the same injection velocity of 0.5 m/s, the small variations in mass injection between the scenarios were due to varying dispersive and diffusive fluxes at the injection boundary. Higher mass injection in scenario 8 arises due to the highest porosity resulting from intense mineral dissolution taking place near the inlet boundary, resulting in increasing dispersive fluxes.

CO_2-saturated brine injected in the reservoir initiated the dissolution of minerals, mainly in close vicinity to the injection boundary (top-left of the reservoir domain). Over time, the reaction zone advanced in the lateral and downward directions. The involved carbonate minerals (calcite, dolomite and siderite) either dissolved or precipitated depending upon the evolving geochemical conditions in the reservoir driven by higher concentration of dissolved CO_2 in the injected brine. Over the period of time, dissolution and precipitation of minerals caused variations in porosity and permeability of the porous media. Fig. 16 presents the porosity variations in the reservoir, close to the injection point, for various reactive transport scenarios after 10

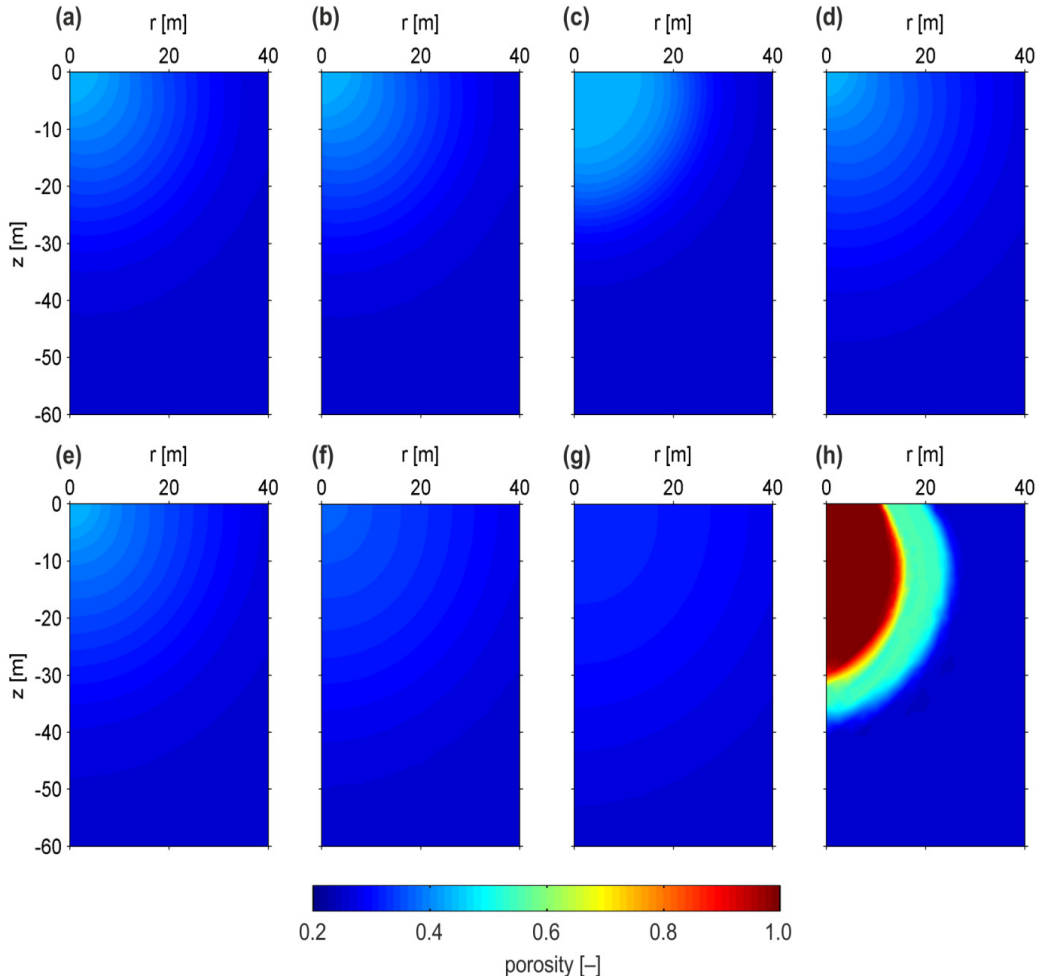

Fig. 16. Variations in medium porosity from the initial porosity of 0.25 for various reactive transport scenarios; (a) scenario 1, (b) scenario 2, (c) scenario 3, (d) scenario 4, (e) scenario 5, (f) scenario 6, (g) scenario 7, and (h) scenario 8 (Paper IV).

years. In scenarios 1 to 5, with the exception of its spread, the medium porosity reached a value of 0.44 from its initial value of 0.25, mainly close to the injection point (Fig. 16a to e). The lower temperature considered in scenario 6 decreased the mineral dissolution and lowered the increase in medium porosity (0.37) in this scenario compared to scenarios 1 to 5. The lowest temperature considered at the injection boundary and its transfer in the reservoir in scenario 7 caused the lowest mineral dissolution and thus the lowest increase in medium porosity (up to 0.32). The defined mineral reactions as a function of the solution pH in scenario 8 caused almost complete dissolution of minerals, resulting in the highest porosity, which reached to nearly unity (upper porosity limit of 0.999). An increase in permeability also resulted from mineral dissolution. In scenario 8, the medium permeability reached a value of 1.33×10^{-5} m^2 from an initial value of 6.46×10^{-13} m^2 (not shown in results).

The dissolution of carbonate minerals in the reservoir, driven by the injected CO_{2aq}, converted the mass of CO_{2aq} into H^+, HCO_3^- and other associated bicarbonate ions (ionic trapping). The net

conversion of injected CO_{2aq} resulted from higher carbonate mineral dissolution compared to their negligible precipitation in the considered carbonate reservoir. Fig. 17 presents the trends of CO_{2aq} mass injected and its consumption in reactions in the reservoir over the period of 10 years. In injection scenarios 1 to 8, the cumulative consumption of CO_2 in the reactions was found to be 1.95×10^4, 2.28×10^4, 1.44×10^4, 2.57×10^4, 2.56×10^4, 2.57×10^4, 2.60×10^4, and 3.97×10^4 tonnes, respectively (Fig. 17c, d and Table 24). The corresponding percentage consumption of CO_2 in scenarios 1 to 8 was found to be 9.61%, 11.09%, 7.17%, 11.72%, 11.76%, 11.83%, 11.97% and 16.46%, respectively, relative to its total mass injected in the reservoir (Fig. 17e, f and Table 24).

Including the sorption process in scenario 2 caused higher CO_2 conversion in reactions compared to that in the corresponding no-sorption scenario 1. Although the cumulative conversion of CO_2 in reactions in the sorption scenario 2 stays higher than that in scenario 1 (Fig. 17b), different trends are found for the percentage conversion (Fig. 17e) in these scenarios over time. The percentage consumption is lower in scenario 2 compared to scenario 1 in the

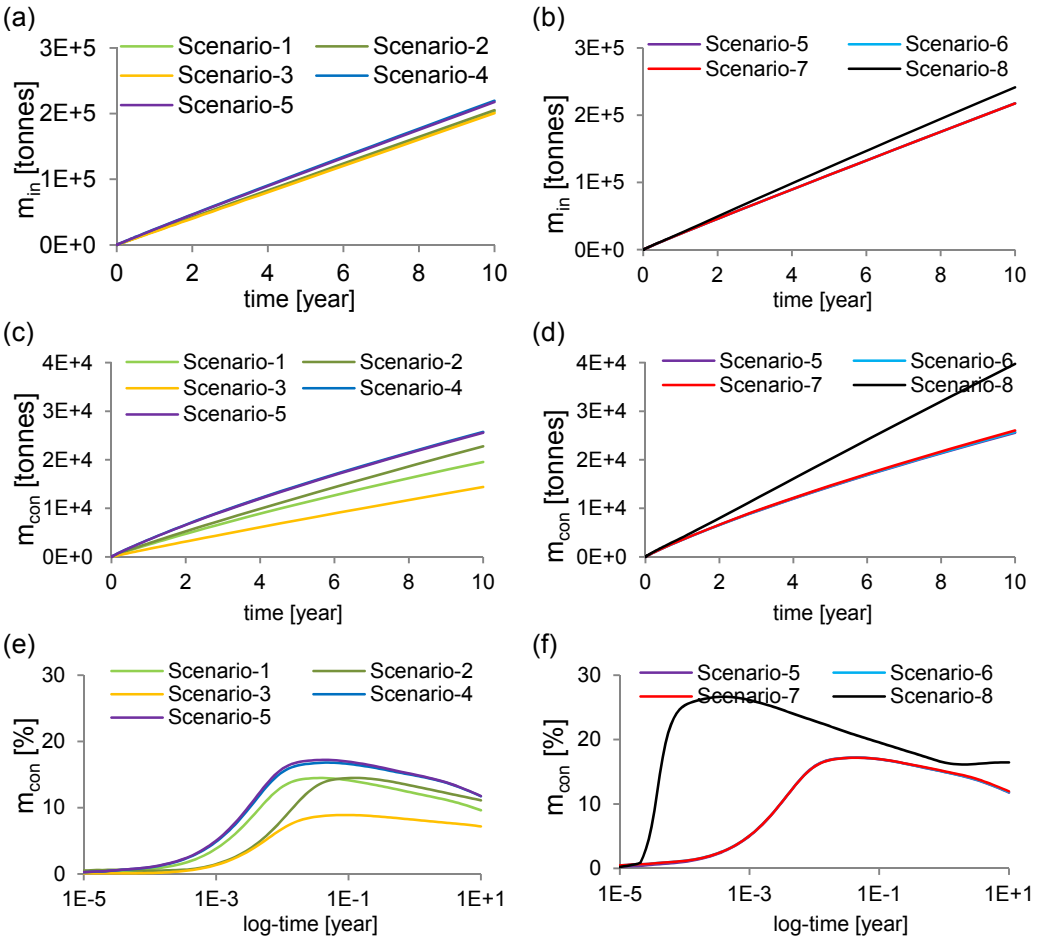

Fig. 17. Mass balance of CO_{2aq} in the reservoir; (a) mass injected in the reservoir in scenarios 1 to 5, (b) mass injected in the reservoir in scenarios 5 to 8, (c) cumulative mass consumption in scenarios 1 to 5, (d) cumulative mass consumption in scenarios 5 to 8, (e) percent mass consumption in scenarios 1 to 5, and (f) percent mass consumption in scenarios 5 to 8 (Paper IV).

Table 24. Mass [tonnes] balance of CO_{2aq} in various injection scenarios after 10 years.

Injection scenarios	Scenario 1	Scenario 2	Scenario 3	Scenario 4	Scenario 5	Scenario 6	Scenario 7	Scenario 8
Total mass injected in the reservoir	2.04×10^{5}	2.05×10^{5}	2.01×10^{5}	2.20×10^{5}	2.18×10^{5}	2.18×10^{5}	2.17×10^{5}	2.42×10^{5}
Mass entering due to advection	2.00×10^{5}	2.00×10^{5}	2.00×10^{5}	2.00×10^{5}	2.00×10^{5}	2.00×10^{5}	2.00×10^{5}	2.00×10^{5}
Mass entering due to diffusion	2.77×10^{-6}	4.07×10^{-6}	3.62×10^{-6}	7.43×10^{-6}	6.70×10^{-6}	6.04×10^{-6}	5.60×10^{-6}	4.68×10^{-5}
Mass entering due to dispersion	3.50×10^{3}	5.24×10^{3}	7.14×10^{2}	1.96×10^{4}	1.75×10^{4}	1.75×10^{4}	1.75×10^{4}	4.15×10^{4}
Mass leaving the domain (bottom boundary)	7.24×10^{3}	6.50×10^{1}	2.92×10^{3}	1.12×10^{4}	9.57×10^{3}	9.59×10^{3}	9.57×10^{3}	0.00
Mass leaving the domain (right-side boundary)	3.39×10^{1}	3.16×10^{1}	3.51×10^{1}	3.37×10^{1}	3.38×10^{1}	3.09×10^{1}	3.09×10^{1}	6.02×10^{1}
Mass stored in an aqueous state	1.77×10^{5}	5.91×10^{4}	1.84×10^{5}	1.82×10^{5}	1.84×10^{5}	1.84×10^{5}	1.83×10^{5}	2.03×10^{5}
Mass stored in an adsorbed state	0.00	1.24×10^{5}	0.00	0.00	0.00	0.00	0.00	0.00
Mass consumed in geochemical reactions	1.95×10^{4}	2.28×10^{4}	1.44×10^{4}	2.57×10^{4}	2.56×10^{4}	2.57×10^{4}	2.60×10^{4}	3.97×10^{4}
Mass uptake of CO_{2aq} (%)	9.61	1.11×10^{1}	7.17	1.17×10^{1}	1.18×10^{1}	1.18×10^{1}	1.20×10^{1}	1.65×10^{1}
Error in mass balance (%)	-1.84×10^{-1}	-1.08×10^{-1}	-4.56×10^{-1}	1.94×10^{-1}	-6.36×10^{-1}	-6.44×10^{-1}	-6.44×10^{-1}	-4.85×10^{-1}
Mass leaving the domain (%)	3.57	4.71×10^{-2}	1.47	5.10	4.41	4.42	4.41	2.49×10^{-2}

initial period, whereas it becomes higher in the former than the latter scenario towards the end of the simulation period (Section 4.2.1.1 is referred for related explanation). Sorption also caused partitioning of injected CO_{2aq} into the aqueous phase (28.78%) and the adsorbed phase (60.20%).

Role of dispersivity and temperature

The lowest mass inflows and lowest CO_2 conversion in scenario 3 are due to the lowest dispersivity being used compared to the rest of the scenarios (Fig. 17a and c). Alternately, the higher inflows and higher CO_2 conversion in scenario 5 are due to the higher dispersivity compared to the corresponding scenarios 1, 3 and 4 (Fig. 17a and c).

The simulation results indicate that the temperature has little effect on the levels of CO_2 consumption in reactions in scenarios 5, 6 and 7 (Fig. 17d and f). In scenario 7, the lowest temperature of 7°C was considered at the inlet boundary, and its transfer into the reservoir lowered the reaction rate constants of minerals, resulting in the lowest mineral dissolution of all scenarios. Alternately, the lower temperature increased the reaction equilibrium constant of minerals. In scenario 7, the equilibrium constants were found to be 93.07, 1409.9 and 1.32 for the minerals calcite, dolomite and siderite, respectively, at 7°C compared to the corresponding values of 48.36, 283.91 and 0.55 at 27°C. The resulting increase in equilibrium constants of minerals keeps the brine solution at a relatively lower saturation state with respect to minerals compared to the scenarios with higher temperatures. Due to the lower temperature, the saturation state of the solution with respect to the minerals attains unity at a relatively higher concentration of reaction products (e.g., Ca^{2+} and HCO_3^- for calcite) and lower concentration of reactant (H^+) compared to the cases with higher temperatures. A decrease in temperature thus causes overall higher mineral dissolution with the associated higher conversion/consumption of H^+ and thus CO_{2aq} in reactions. Thus, in the lower temperature scenarios 6 and 7, the effect of higher mineral dissolution (a result of lower saturation states) dominates the effect of lower mineral reaction rates and resulted in slightly higher mineral dissolution, pore volume and consumption of CO_{2aq} in reactions compared to those found in scenario 5 (Table 24).

Role of mineral kinetics defined as a function of the solution pH

The highest mineral dissolution with the associated highest porosity and CO_{2aq} conversion in scenario 8 is due to the mineral kinetic reactions being defined as a function of the solution pH. For example, the kinetic reaction rate of the mineral calcite, defined as a function of pH, was found to be 7.13×10^{-5} mol/(s-m^2) compared to its value of 1.79×10^{-9} mol/(s-m^2) if its reaction rate was defined independent of the solution pH. Thus, fast mineral reaction rates caused almost complete mineral dissolution, causing the medium porosity to reach nearly unity, especially close to the injection boundary. Additionally, in scenario 8, a decrease in

porosity was found at some locations in the reservoir due to mineral precipitation (0.20 from an initial value of 0.25).

5. CONCLUSIONS

This doctoral thesis focuses on the reactive transport modelling of leaking CO_{2aq} along the migrating pathway in fractured bedrock. The first three papers were aimed at analysing the reactive transport of CO_{2aq} as it is leaking from the reservoir along a conducting fractured pathway in the caprock. In the fourth paper, a relatively safer mode of CO_2 sequestration is investigated, wherein CO_2 is injected in dissolved phase in brine in the subsurface carbonate reservoir. For these purposes, a geochemical code was developed and implemented in COMSOL. For the considered geochemical system, the presented model is capable of efficiently solving the reactive transport of dissolved CO_2 in the porous media, considering the coupling between transport and geochemical reactions and related variations in hydrological and transport properties.

Findings related to the leakage of dissolved CO_2:

- The mobility and spread of dissolved CO_2 along the leakage pathway is found to be controlled by complex interactions between number of transport-reaction mechanisms that has not been realized before: (i) advection, dispersion and diffusion; (ii) sorption; and (iii) geochemical reactions.
- For the simulated scenarios, storage in aqueous and adsorbed states caused significant retardation in transport of leaking CO_{2aq}. Consumption of CO_{2aq} in geochemical reactions caused additional transport retardation.
- Leaking CO_{2aq} travelled less than a distance of 250 m along the fractured pathway in 500 years, for a fluid velocity of nearly 20 m/year in the fracture, due to retardation caused by mass stored in aqueous and adsorbed states and consumed in reactions.
- Leaking brine saturated with dissolved CO_2 caused dissolution and precipitation of carbonate minerals with significant increase in the medium porosity and permeability along the main leakage pathway.
- Dissolution of carbonate minerals converted dissolved CO_2 into other ions and thereby reduced the dissolved content of CO_2 mass along the travel pathway.
- Inclusion of sorption in the model analysis induced higher consumption of CO_2 in geochemical reactions. The use of a partition coefficient of 2.50×10^{-4} m^3/kg caused nearly 131% higher CO_2 consumption in reactions compared to the case with no sorption.
- Advection in the low permeable cap rock can under certain (plausible) conditions increase the leakage of CO_{2aq} that generally occurs from the reservoir through sparse fractures by approximately 305%. Similarly, such an

advective transport scenario caused nearly a 12% higher consumption of CO_2 in reactions than was noted in the scenario where transport of CO_{2aq} was through diffusion alone in the rock matrix.

- Increasing the fluid vertical velocity three times decreased CO_2 consumption by approximately 28% (from 0.78% to 0.56% of leakage mass), whereas increasing the dispersivity three times caused an increased consumption by 31% (from 0.78% to 1.02% of leakage mass).
- Geochemical reactions and increase in temperature due to heat transport by leaking brine played a significant role in the consumption of leaking CO_{2aq} along the travel pathway. Considering the extended geochemical system resulted in an approximately 11% higher consumption of CO_2 in reactions compared to the simplified geochemical system. The inclusion of heat transport by leaking brine along the leakage pathway caused 14% higher CO_2 conversion in reactions compared to the scenario where constant temperature was assumed along the transport pathway.

Findings related to injection of dissolved CO_2 in the subsurface carbonate reservoir:

- Injection of CO_2-saturated brine caused intense and complete dissolution of carbonate minerals near the injection point, where the porosity reached nearly unity. Over the injection period of 10 years, a maximum of 16.5% of the dissolved CO_2 injected in the reservoir was found to be consumed in geochemical reactions by its conversion into other ions.
- Immediate and significant conversion of dissolved CO_2 in reactions enhanced the storage safety.

6. STUDY LIMITATIONS AND FUTURE WORK

Although sorption is found to be an important mechanism for the fixation of CO_{2aq}, uncertainties exist regarding the sorption properties of CO_2 on the surfaces of various minerals and rock formations. Thus, there is a need for proper evaluation of sorption characteristics of CO_2 on various minerals and rocks for precise quantification of the CO_{2aq} mass stored in an adsorbed state.

Though this study provided an estimate of the conversion levels of leaking CO_{2aq} along the travel pathway, only fast-reacting carbonate minerals were included in the modelling for geochemical interactions. Relatively higher conversion levels of CO_{2aq} would be expected if multi-mineralogical systems were included in addition to the considered carbonate minerals.

Thus, future reactive transport modelling of CO_{2aq} should include sandstone or basalt minerals to represent higher and permanent consumption of CO_{2aq} in the form of mineral trapping. However, to perform the reactive transport modelling involving Al^{3+}-bearing minerals, there is a need to improve the numerical solution methods for the governing equations.

References

Ahmad N, Wörman A, Bottacin-Busolin A, Sanchez-Vila X. 2015. Reactive transport modeling of leaking CO_2-saturated brine along a fractured pathway. *Int. J. Greenhouse Gas Cont.* **42**, 672-689.

Alfredsson HA, Oelkers EH, Hardarsson BS, Franzson H, Gunnlaugsson E, Gislason SR. 2013. The geology and water chemistry of the Hellisheidi, SW-Iceland carbon storage site. *Int. J. Greenhouse Gas Cont.* **12**, 399-418.

Al-Rawajfeh AE. 2004. *Modelling and Simulation of CO_2 Release in Multiple-Effect Distillers for Seawater Desalination*. Halle-Wittenberg, Halle (Saale), Germany.

Andreani M, Gouze P, Luquot L, Jouanna P. 2008. Changes in seal capacity of fractured claystone caprocks induced by dissolved and gaseous CO_2 seepage. *Geophys Res. Lett.* **35**(L 14404).

Aradóttir ESP, Sonnenthal EL, Björnsson G, Jónsson H. 2012. Multidimensional reactive transport modeling of CO_2 mineral sequestration in basalts at the Hellisheidi geothermal field, Iceland. *Int. J. Greenhouse Gas Cont.* **9**:24-40.

Audigane P, Gaus I, Czernichowski-Lauriol I, Pruess K, Xu T. 2007. Two-dimensional reactive transport modeling of CO_2 injection in a saline aquifer at the Sleipner site, North Sea. *Am. J. Sci.* **307**:974-1008.

Bachu S, Adams JJ. 2003. Sequestration of CO_2 in geological media in response to climate change: capacity of deep saline aquifers to sequester CO_2 in solution. *Energy Convers. and Manage.* **44**:3151-3175.

Bachu S, Gunter WD, Perkins EH. 1994. Aquifer Disposal of CO_2: Hydrodynamic and Mineral Trapping. *Energy Convers. and Manage.* **35(4)**:269-279.

Basirat F, Sharma P, Fagerlund F, Niemi A. 2015. Experimental and modeling investigation of CO2 flow and transport in a coupled domain of porous media and free flow. *Int. J. Greenhouse Gas Cont.* **42**, 461-470.

Bear J, Bachmat Y. 1990. *Introduction to Modeling of Transport Phenomena in Porous Media.* Kluwer Academic Publishers, Dordrecht, The Netherlands.

Bear JJ, Cheng HDA. 2010. *Modeling Contaminant Transport*. 341-523.

Bethke CM. 2008. *Geochemical and Biogeochemical Reaction Modeling.* Cambridge University Press, United States of America.

Bodin J, Delay F, de Marsily G. 2003. Solute transport in a single fracture with negligible matrix permeability: 2. mathematical formalism. *Hydrogeol. J.* **11**:434-454.

CO2-DISSOLVED: Storing industrial CO_2 emissions while producing geothermal energy for local use. *The French Geological Survey*. http://co2-dissolved.brgm.fr/.

COMSOL. *The Platform for Physics-Based Modeling and Simulation.* COMSOL Inc. AB, Stockholm, Sweden. http://www.comsol.com/.

Cvetkovic V, Selroos JO , Cheng H. 1999. Transport of reactive tracers in rock fractures. *J. Fluid Mech.* **378**:335-356.

Chabonan M., David B, Boyeau B. 2015. Averaged model for momentum and dispersion in hierarchical porous media. *Phys. Rev. E* **92(2)**, 023201.

Delany JM, Lundeen SR. 1990. *The LLNL thermochemical database*. Lawrence Livermore National Laboratory Report UCRL-21658, 150 p.

Dilmore RM, Allen DE, Jones JRM, Hedgen SW, Soong Y. 2008. Sequestration of dissolved CO_2 in Oriskany Formation. *Environ. Sci. Technol.* **42**: 2760-2766.

Dreybrodt W, Eisenlohr L, Madry B, Ringer S. 1997. Precipitation kinetics of calcite in the system $CaCO_3$-H_2O-CO_2: The conversion to CO_2 by the slow process $H^+ + HCO_3^- \rightarrow CO_2 + H_2O$ as a rate limiting step. *Geochim. Cosmochim. Ac.* **61(18)**:3897-3904.

Dreybrodt W, Lauckner J, Zaihua L, Svensson U, Buhmann D. 1996. The kinetics of the reaction in the $CO_2 + H_2O \rightarrow H^+ + HCO_3^-$ as one of the rate limiting steps for the

dissolution of calcite in the system H_2O-CO_2-$CaCO_3$. *Geochim Cosmochim. Ac.* **60(18)**:3375-3381.

Duan Z, Hu J, Li D, Mao S. 2008. Densities of the CO_2-H_2O and CO_2-H_2O-NaCl systems up to 647 K and 100 MPa. *Energ. Fuel.* **22(3)**:1666-1674.

Duan Z, Sun R. 2003. An improved model calculating CO_2 solubility in pure water and aqueous NaCl solutions from 273 to 533 K and from 0 to 2000 bar. *Chem. Geol.* **193**:257-271.

Duan Z, Sun R, Zhu C, Chou I-M. 2006. An improved model for the calculation of CO_2 solubility in aqueous solutions containing Na^+, K^+, Ca^{2+}, Mg^{2+}, Cl^-, and SO_4^{2-}. *Mar. Chem.* **98(2-4)**:131–139.

Eke PE, Naylor M, Haszeldine S, Curtis A. 2011. CO_2/brine surface dissolution and injection: CO_2 storage enhancement. *SPE Projects, Facilities Const.* **March 2011.** 41-53.

Ellis BR, Bromhal GS, McIntyre DL, Peters CA. 2011a. Changes in caprock integrity due to vertical migration of CO_2-enriched brine. *Energy Procedia* **4**:5327-5334.

Ellis B, Peters C, Fitts J, Bromhal G, McIntyre D, Warzinski R, Resenbaum E. 2011b. Deterioration of a fractured carbonate caprock exposed to CO_2-acidified brine flow. *Greenhouse Gases: Sci. Technol.* **1**:248-260.

Fields PA, Graham JB, Rosenblatt RH, Somero GN. 1993. Effects of expected global climate change on marine faunas. *Trends Ecol. Evol.* **8(10)**:361-367.

Freeze RA, Cherry JA. 1979. *Groundwater.* Prentice Hall, Englewood Cliffs, N.J.

Fujii T, Nakagawa S, Sato Y, Inomata H, Hashida T. 2010. Sorption characteristics of CO_2 on rocks and minerals in storing CO_2 processes. *Nat. Resour.* **01(01)**:1-10.

García JE. 2003. *Fluid Dynamics of carbon dioxide disposal into saline aquifers,* PhD thesis. University of California, Berkeley.

Gaus I. 2010. Role and impact of CO_2–rock interactions during CO_2 storage in sedimentary rocks. *Int. J. Greenhouse Gas Cont.* **4(1)**:73-89.

Gaus I, Azaroual M, Czernichowski-Lauriol I. 2005. Reactive transport modelling of the impact of CO_2 injection on the clayey cap rock at Sleipner (North Sea). *Chem. Geol.* **217**:319-337.

Gherardi F, Xu T, Pruess K. 2007. Numerical modeling of self-limiting and self-enhancing caprock alteration induced by CO_2 storage in a depleted gas reservoir. *Chem. Geol.* **244(1-2)**:103-129.

Gislason SR, Oelkers EH. 2014. Carbon Storage in Basalt. Sci. **344**:373-374.

Golfier F., Lasseux D, Quintard M. 2015. Investigation of the effective permeability of vuggy or fractured porous media from a Darcy-Brinkman approach. *Computat. Geosci.* **19**, 63-78.

Grisak GE, Pickens JF. 1980. Solute transport through fractured media 1. The effect of matrix diffusion. *Water Resour. Res.* **16(4)**:719-730.

Gulbransen AF, Hauge VL, Lie K-A. 2010. A multiscale mixed finite-element method for vuggy and naturally-fractured reservoirs. *SPE J.* **15(2)**:395-403.

Hassanzadeh H, Pooladi-Darvesh M, Elsharkawy AM, Keith DW, Leonenko Y. 2008. Predicting PVT data for CO_2–brine mixtures for black-oil simulation of CO_2 geological storage. *Int. J. Greenhouse Gas Cont.* **2**:65-77.

Haugan PM, Joos F. 2004. Metrics to assess the mitigation of global warming by carbon capture and storage in the ocean and in geological reservoirs. *Geophys. Res. Lett.* **31**(L18202).

Heller R, Zoback M. 2014. Adsorption of methane and carbon dioxide on gas shale and pure mineral samples. *J. Unconven. Oil Gas Resour.* **8**:14-24.

Holloway S. 1997. An overview of the underground disposal of carbon dioxide. *Energy Conv. Manage.* **38(Suppl)**:S193-S198.

Holloway S. 2005. Underground sequestration of carbon dioxide-a viable greenhouse gas mitigation option. *Energy.* **30**:2318-2333.

IPCC. 2002. Workshop on carbon dioxide capture and storage. *Proceedings, Regina, Canada.*

IPCC, 2005. *IPCC Special Report on Carbon Dioxide Capture and Storage*. Cambridge University Press, Cambridge, United Kingdom and New York, NY, USA.

Johnson JW, Nitao JJ, Knauss KG. 2004. Reactive transport modelling of CO_2 storage in saline aquifers to elucidate fundamental processes, trapping mechanisms, and sequestration partitioning. *Geological Society of London Special Publication on Carbon Sequestration Technologies*. UCRL-JRNL-205627.

Kaufmann G, Dreybrodt W. 2007. Calcite dissolution kinetics in the system $CaCO_3$–H_2O–CO_2 at high undersaturation. *Geochim. Cosmochim Ac.* **71(6)**:1398-1410.

Lai K-H, Chen J-S, Liu C-W, Yang S-Y. 2014. Effect of permeability–porosity functions on simulated morphological evolution of a chemical dissolution front. *Hydrol. Process.* **28**:16-24.

Lasaga AC. 1984. Chemical kinetics of water-rock interaction. *J. Geophys. Res.* **89(B6)**:4009-4025.

Lasaga AC, Soler JM, Ganor J, Bruch TE, Nagy KL. 1994. Chemical weathering rate laws and global geochemical cycles. *Geochim. Cosmochim. Ac.* **58(10)**:2361-2386.

Laubach SE, Olson JE, Eichhubl P, Fomel S, Marrett RA. 2010. Natural Fractures from the perspective of diagenesis. *Canadian Society of Exploration Geophysicists, CSEG RECORDER*, September 2010.

Leonenko Y, Keith DW. 2008. Reservoir engineering to accelerate the dissolution of CO_2 stored in aquifers. *Environ. Sci. Technol.* **42**:2742–2747.

Li D, Graupner BJ, Bauer S. 2011. A method for calculating the liquid density for the CO_2-H_2O-NaCl system under CO_2 storage condition. *Energy Procedia.* **4**:3817-3824.

Liu C, Zhang R, Zhang H, Yang X., Wang J. 2013. Characteristics and origin of Microfracture in Lower Cretaceous Tight Sandstone from Kuqa Foreland Basin, NW China. *AAPG Annual Convention and Exhibition, Pittsburgh, Pennsylvania*, May 19-22, 2013.

Mao S, Duan Z. 2009. The viscosity of aqueous alkali-chloride solutions up to 623 K, 1000 bar, and high ionic strength. *Int. J. Thermophys.* **30(5)**:1510-1523.

MATLAB. *The Language of Technical Computing.* MathWorks®. http://se.mathworks.com/products/matlab/.

Middleton RS, Keating GN, Stauffer PH, Jordan AB, Viswanathan HS, Kang QJ. 2012. The cross-scale science of CO_2 capture and storage: from pore scale to regional scale. *Energy Environ. Sci.* **5(6)**:7328-7345.

Neretnieks I. 1980. Diffusion in the rock matrix: an important factor in radionuclide retardation? *J. Geophys. Res.* **85(B8)**:4379-4397.

Nogues JP, Fitts JP, Celia MA, Peters CA. 2013. Permeability evolution due to dissolution and precipitation of carbonates using reactive transport modeling in pore networks. *Water Resour. Res.* **49**:6006-6021.

Novak CF. 1993. Modeling mineral dissolution and precipitation in dual-porosity fracture-matrix system. *J. Contam. Hydrol.* **13(1-4)**:91-115.

Novak CF. 1996. Development of the FMT chemical transport simulator: coupling aqueous density and mineral volume fraction to phase compositions. *J. Contam. Hydrol.* **21(1-4)**:297-310.

Orr JR. FM. 2009a. CO_2 capture and storage: are we ready? *Energy Environ. Sci.* **2(5)**:449-458.

Orr JR. FM. 2009b. Onshore geological storage of CO_2. *Science.* **325**:1656-1658.

Palandri JL, Kharaka YK. 2004. A compilation of rate parameters of water-mineral interaction kinetics for application to geochemical modeling. *U.S. Geological Survey*, Open File Report 2004-1068.

Parkhurst DL, Appelo CAJ. 2013. Description of input and examples for PHREEQC Version 3-A computer program for speciation, batch-reaction, one-dimensional transport, and inverse geochemical calculations. *U.S.Geological Survery* Techniques and Methods, 6-A43.

Pool M. Carrera J, Vilarrasa V, Silva O, Ayora C. 2013. Dynamics and design of systems for geological storage of dissolved CO_2. *Adv. Water Resour.* **62**:533-542.

Popov P, Efendiev Y, Qin G. 2009. Multiscale modelling and simulations of flows in naturally fractured karst reservoirs. *Commun. Comput. Phys.* **6(1)**:162-184.

Pruess K. 2005. Numerical studies of fluid leakage from a geologic disposal reservoir for CO_2 show self-limiting feedback between fluid flow and heat transfer. *Geophys. Res. Lett.* **32**(L14404).

Pruess K. 2008. Leakage of CO_2 from geologic storage: role of secondary accumulation at shallow depth. *Int. J. Greenhouse Gas Contr.* **2(1)**:37-46.

Saaltink MW, Ayora C, Carrera J. 1998. A mathematical formulation for reactive transport that eliminates mineral concentrations. *Water Resou. Res.* **34(7)**:1649-1656.

Sajjadi B, Abdul Aziz AR, Baroutian S, Ibrahim S. 2014. Investigation of convection and diffusion during biodiesel production in packed membrane reactor using 3D simulation. *J. Ind. Eng. Chem.* **20:**1493-1504.

Santschi C, Rossi MJ. 2006. Uptake of CO_2, SO_2, HNO_3 and HCl on calcite ($CaCO_3$) at 300 K: mechanism and the role of adsorbed water. *J. Phys. Chem. A* **110(21)**:6789-6802.

Song Y, Chen B, Nishio M, Akai M. 2005. The study on density change of carbon dioxide seawater solution at high pressure and low temperature. *Energy.* **30**:2298–2307.

Steefel CI, Lasaga AC. 1994. A coupled model for transport of multiple chemical species and kinetic precipitation/dissolution reactions with application to reactive flow in single phase hydrothermal systems. *Ame. J. sci.* **294**:529-592.

Steefel CI, Lichtner PC. 1998a. Multicomponent reactive transport in discrete fractures I: Controls on reaction front geometry. *J. Hydrol.* **209(1-4)**:186-199.

Steefel CI, Lichtner PC. 1998b. Multicomponent reactive transport in discrete fractures II: Infiltration of hyperalkaline groundwater at Maqarin, Jordan, a natural analogue site. *J. Hydrol.* **209(1-4)**:200-224.

Stone EJ, Lowe JA, Shine KP. 2009. The impact of carbon capture and storage on climate. *Energy Environ. Sci.* **2(1)**:81-91.

Svensson U, Dreybrodt W. 1992. Dissolution kinetics of natural calcite minerals in CO_2-water systems approaching calcite equilibrium. *Chem. Geol.* **100**:129-145.

The GEOCHEMIST'S WORKBENCH. *An integrated geochemical modeling package.* Aqueous Solutions LLC, Champaign, IL 61820 USA. https://www.gwb.com/.

TOTAL S.A. http://www.total.com/en/society-environment/environment/climate-and-carbon/carbon-capture-and-storage/challenges/carbon-capture-and-geological-storage-co2-whats-it-all-about. (Accessed 20160310).

Wealthall GP, Steele A, Bloomfield JP, Moss RH, Lerner DN. 2001. Sediment filled fractures in the Permo-Triassic sandstones of the Cheshire basin: observations and implications for pollutant transport. *J. Contam. Hydrol.* **50:**41-51.

Weir GJ, White SP, Kissling WM. 1996. Reservoir storage and contamination of greenhouse gases. *Transp. Porous Media.* **23(1)**:37-60.

Wolf-Gladrow DA, Riebesell U, Brukhardt S, Bijma J. 1999. Direct effects of CO_2 concentration on growth and isotopic composition of marine plankton. *Tellus.* **51B(2)**:461-476.

Wu Y-S, Ye M, Sudicky EA. 2010. Fracture-flow-enhanced matrix diffusion in solute transport through fractured porous media. *Transport Porous Med.* **81**:21-34.

Xu S, Wörman A, Dverstorp B. 2001. Heterogeneous matrix diffusion in crystalline rock-implications for geosphere retardation of migrating radionuclides. *J. Contam. Hydrol.* **47(2-4)**:365-378.

Xu T, Apps JA, Preuss K. 2003. Reactive geochemical transport simulation to study mineral trapping for CO_2 disposal in deep arenaceous formations. *J. Geophys. Res.* **108(B2)**:2071.

Xu T, Apps JA, Pruess K. 2004. Numerical simulation of CO_2 disposal by mineral trapping in deep aquifers. *Appl. Geochem.* **19(6)**:917-936.

Xu T, Apps JA, Pruess K. 2005. Mineral sequestration of carbon dioxide in a sandstone-shale system. *Chem. Geol.* **217**: 295-318.

Xu T, Apps JA, Pruess K, Yamamoto H. 2007. Numerical modeling of injection and mineral trapping of CO_2 with H_2S and SO_2 in a sandstone formation. *Chem. Geol.* **242**:319-346.

Xu T, Pruess K. 2001. Modeling multiphase fluid flow and reactive geochemical transport in variably saturated fractured rocks: 1. Methodology. *Ame. J. Sci.* **301**:16-33.

Yeh G-T, Tripathi VS. 1991. A model for simulating transport of reactive multispecies components: model development and demonstration. *Water Resour. Res.* **27(12)**:3075-3094.

Zerai B, Saylor BZ, Matisoff G. 2006. Computer simulation of CO_2 trapped through mineral precipitation in the Rose Run Sandstone, Ohio. *Appl. Geochem.* **21**:223–240.

Zhang D, Song J. 2014. Mechanisms for geological carbon sequestration. *Procedia IUTAM.* **10**:319-327.

Zhang Y, Cheng F, Song Y, Zhao J, Zhan Y, Jian W. 2011. Density of Carbon Dioxide + Brine Solution from Tianjin Reservoir under Sequestration Conditions. *J. Chem. Eng. Data* **56**:565-573.

7. APPENDIX A: MINERAL'S CONCENTRATION, REACTIVE SURFACE AREA, SPECIFIC SURFACE AREA AND DENSITY OF THE MEDIUM

The methodology of computing the mineral's reactive surface area and other associated relations is based on geometric approach. In the first step, initial values (denoted by subscript 0) of the parameters are calculated followed by computation of their space and time dependent variations.

7.1. Initial values

The volume fraction of the individual solid mineral ($VF_{m,s,0}$) is related to the porous volume fraction of the individual mineral ($VF_{m,p,0}$) based on the following relationship:

$$VF_{m,s,0} = {VF_{m,p,0}}\Big/{VF_{rock,p,0}} \quad \text{(A.1)}$$

where the term "$VF_{rock,p,0} = \sum VF_{m,p,0}$" represents the sum of the porous volume fractions of all minerals forming the porous media. The volume [m^3] of the solid rock formation composed of various minerals ($V_{rock,s,0}$) exposed to the pore volume [m^3] occupied by one kg of water ($V_{pore,0}$) is found from the following relation:

$$V_{rock,s,0} = V_{pore,0}\left({1}\Big/{\theta_0} - 1\right) \quad \text{(A.2)}$$

where θ_0 is the initial porosity of the medium and $V_{pore,0}$ is calculated from the following relationship:

$$V_{pore,0} = {1}\Big/{\rho_b} \quad \text{(A.3)}$$

where ρ_b is the density [kg/m^3] of brine fluid. The solid volume [m^3] of an individual mineral ($Vm,s,0$) exposing per kg of water is found from the total solid rock volume as follows:

$$Vm,s,0 = VF_{m,s,0}V_{rock,s,0} \quad \text{(A.4)}$$

The number of moles of solid mineral per kg of water is calculated from the following relationship:

$$c_{m,s,0} = V_{m,s,0}/MV_m \quad \text{(A.5)}$$

where MV_m [m^3/mol] is the molar volume of the mineral. The number of individual mineral grains is obtained from the following relationship:

$$N_{m,g,0} = V_{m,s,0}/V_{m,g} \quad \text{(A.6)}$$

The surface area of the mineral per kg of water [m^2/(kg water)] is found from the following relationship:

$$A_{m,SA,0} = N_{m,g,0}A_{m,g} \quad \text{(A.7)}$$

The surface area and the volume of the mineral grains are related to the mineral grain radius by assuming the spherical grains, as follows:

$$\begin{cases} A_{m,g} = 4\pi r_g^2 \\ V_{m,g} = 4/3\pi r_g^3 \end{cases} \quad \text{(A.8)}$$

The reactive surface area of the mineral is a fraction of the surface area. By assuming this ratio as 10%, we can express the reactive surface per kg of water [m^2/(kg water)] as follows:

$$A_{m,RSA,0} = 0.1 A_{m,SA,0} \quad \text{(A.9)}$$

The specific surface area of the rock per cubic meter of solid rock required for the calculation of the medium permeability is found from the following relationship:

$$A_{rock,SSAV,0} = \sum A_{m,SSAV,0} \quad \text{(A.10)}$$

where $A_{m,SSAV,0}$ is the specific surface area of an individual mineral per cubic meter of solid rock and is calculated from the following relationship:

$$A_{m,SSAV,0} = A_{m,SA,0} VF_{m,s,0} / \left(V_{rock,s,0} VF_{rock,s,0} \right) \quad \text{(A.11)}$$

Here, the term $VF_{rock,s,0} = \sum VF_{m,s,0}$ represents the sum of the solid volume of all the minerals that constitute the solid rock excluding the porosity. Now, the mineral concentration per cubic meter of bulk volume, which is required for its mass conservation (defined by ODE), is found from the following relationship:

$$c_{m,bulk,0} = n_{m,s,0} / V_{tot,sw,0} \quad \text{(A.12)}$$

where the total bulk volume ($Vtot,sw,0$) which is the sum of the pore volume per kg of water and the volume of solid rock per kg of water, is

$$V_{tot,sw,0} = V_{pore,0} + V_{rock,s,0} \quad \text{(A.13)}$$

The density of the non-porous medium, which is composed of various minerals, is found from the following relationship:

$$\rho_{rock,s,0} = \sum \rho_{m,s} VF_{m,s,0} \quad \text{(A.14)}$$

7.2. Space and time dependent variations

Changes in the mineral's concentration ($c_{m,bulk}$), due to mineral kinetic reaction, also change the volume fraction of the minerals as follows:

$$VF_{m,p} = \sum c_{m,bulk} MV_m \quad \text{(A.15)}$$

The updated volume fraction of porous rock is found from the following relationship:

$$VF_{rock,p} = \sum VP_{m,p} \quad \text{(A.16)}$$

Change in the medium porosity is computed from the following relationship:

$$\theta = \left(1 - VF_{rock,p} \right) \quad \text{(A.17)}$$

The updated volume fraction of non-porous mineral is calculated as:

$$VF_{m,s} = VF_{m,p} / VF_{rock,p} \quad \text{(A.18)}$$

The updated volume fraction of non-porous rock, which is composed of various minerals, is determined by using the following relationship:

$$VF_{rock,s} = \sum VF_{m,s} \quad \text{(A.19)}$$

The updated volume of non-porous rock per kg of water is computed from the following relationship:

$$V_{rock,s} = V_{pore}\left(1/\theta - 1\right) \quad \text{(A.20)}$$

where the pore volume [m^3] occupied by one kg of water is obtained from the relation:

$$V_{pore} = {1}/{\rho_b} \quad \text{(A.21)}$$

Total bulk volume, which is the sum of the pore volume per kg of water and the volume of solid rock per kg of water, is found from the following relationship:

$$V_{tot,sw} = V_{pore} + V_{rock,s} \quad \text{(A.22)}$$

The mineral solid volume is computed as follows:

$$V_{m,s} = VF_{m,s}V_{rock,s} \quad \text{(A.23)}$$

From the following relationship, we can obtain the number of mineral grains per kg of water:

$$N_{m,g} = V_{m,s}/V_{m,g} \quad \text{(A.24)}$$

The surface area of the mineral per kg of water is updated from the following relationship:

$$A_{m,SA} = N_{m,g}A_{m,g} \quad \text{(A.25)}$$

Accordingly, the reactive surface area of the mineral per kg of water is obtained from the following relationship:

$$A_{m,RSA} = 0.1A_{m,SA} \quad \text{(A.26)}$$

The successive decrease in the concentration of minerals due to their dissolution results in a successive decrease in their reactive surface and in turn the dissolution reaction rate of the minerals. The specific surface area of an individual mineral per cubic meter of solid rock is calculated from the following relationship:

$$A_{m,SSAV} = A_{m,SA}VF_{m,s}/\left(V_{rock,s}VF_{rock,s}\right) \quad \text{(A.27)}$$

The specific surface area of the rock per cubic meter of solid rock that is required for calculating the medium permeability is obtained from the following relationship:

$$A_{rock,SSAV} = \sum A_{m,SSAV} \quad \text{(A.28)}$$

Accordingly, the updated density of the non-porous rock medium is found from the following relationship:

$$\rho_{rock,s} = \sum \rho_{m,s}VF_{m,s} \quad \text{(A.29)}$$

Finally, the updated bulk density of the porous rock medium is found from the following relationship:

$$\rho_{rock,bulk} = (1-\theta)\rho_{rock,s} \quad \text{(A.30)}$$